# Special Report 86-16

July 1986

**US Army Corps
of Engineers**

Cold Regions Research &
Engineering Laboratory

# *Blasting and blast effects in cold regions*

*Part II: Underwater explosions*

Malcolm Mellor

| REPORT DOCUMENTATION PAGE | | READ INSTRUCTIONS BEFORE COMPLETING FORM |
|---|---|---|
| 1. REPORT NUMBER<br><br>Special Report 86-16 | 2. GOVT ACCESSION NO. | 3. RECIPIENT'S CATALOG NUMBER |
| 4. TITLE (and Subtitle)<br><br>BLASTING AND BLAST EFFECTS IN COLD REGIONS<br>Part II: Underwater Explosions | | 5. TYPE OF REPORT & PERIOD COVERED |
| | | 6. PERFORMING ORG. REPORT NUMBER |
| 7. AUTHOR(s)<br><br>Malcolm Mellor | | 8. CONTRACT OR GRANT NUMBER(s) |
| 9. PERFORMING ORGANIZATION NAME AND ADDRESS<br><br>U.S. Army Cold Regions Research and Engineering<br>Laboratory, Hanover, New Hampshire 03755-1290 | | 10. PROGRAM ELEMENT, PROJECT, TASK AREA & WORK UNIT NUMBERS<br>6.27.40A<br>DA Project 4A762730AT42<br>Task Area CS, Work Unit 029 |
| 11. CONTROLLING OFFICE NAME AND ADDRESS<br><br>Office of the Chief of Engineers<br>Washington, D.C. 20314-1000 | | 12. REPORT DATE<br>July 1986 |
| | | 13. NUMBER OF PAGES<br>60 |
| 14. MONITORING AGENCY NAME & ADDRESS(If different from Controlling Office) | | 15. SECURITY CLASS. (of this report)<br><br>Unclassified |
| | | 15a. DECLASSIFICATION/DOWNGRADING SCHEDULE |

16. DISTRIBUTION STATEMENT (of this Report)

Approved for public release; distribution is unlimited.

17. DISTRIBUTION STATEMENT (of the abstract entered in Block 20, if different from Report)

18. SUPPLEMENTARY NOTES

19. KEY WORDS (Continue on reverse side if necessary and identify by block number)

| | | |
|---|---|---|
| Blast waves | Shock waves | Underwater ordnance |
| Cold regions | Underwater explosions | |
| Explosions | Underwater demolition | |

20. ABSTRACT (Continue on reverse side if necessary and identify by block number)

The general characteristics of underwater explosions are reviewed in order to provide a background for the consideration of under-ice explosions. Test data for under-ice explosions and for explosive icebreaking are summarized and interpreted.

PREFACE

This is one of a series of reports that summarize data relating to blasting procedures and blast effects in cold regions. They are organized to deal successively with (1) explosions in air, (2) explosions in water, and (3) explosions i solid ground materials. For the most part, the blasting procedures used in cold regions are not much different from those that are in general use elsewhere. Similarly, the principles involved in assessing blast effects in cold regions are the same as those that apply to blast effects generally. The reports therefore summarize principles and data for general explosions technology, and then present the procedures and data for cold environments within this framework.

The purpose of the series is to provide a convenient reference source for engineers faced with problems of explosions or blasting in cold regions. Because not all engineers are well acquainted with explosions technology, relevant physical principles are explained or summarized, but there is no attempt to explore the underlying theory in depth, nor is there any treatment of the practical aspects of explosives use and safety practices. These topics are covered well in Army Technical Manuals and Army Materiel Command publications, as well as in commercial blasters' handbooks and in textbooks.

This report was prepared by Dr. Malcolm Mellor, Research Physical Scientist, Experimental Engineering Division, U.S. Army Cold Regions Research and Engineering Laboratory. The work was done under DA Project 4A762730-AT42, Design, Construction, and Operations Technology for Cold Regions, Task Area Combat Support, Work Unit 029, Explosives and Projectile Impact Under Winter Conditions.

The author is grateful to Donald Albert for his careful review of the manuscript and suggestions for improvement. The numerous figures were prepared by Edward Perkins and his staff.

CONTENTS

ILLUSTRATIONS

iv

TABLES

# BLASTING AND BLAST EFFECTS IN COLD REGIONS
## PART II: UNDERWATER EXPLOSIONS

Malcolm Mellor

## INTRODUCTION

The close-range effects of a deep underwater explosion in cold regions are not significantly different from those of the same kind of explosion in the waters of temperate or tropical regions. Temperature and salinity, and stratifications of temperature and salinity, have to be taken into account, but the relevant physical considerations are no different from those that are applied for any waters.

The special feature that distinguishes the waters of cold regions from those in other parts of the world is ice. With an undisturbed cover of recently formed ice, the water surface is sealed by a solid floating plate. Other types of ice covers may consist of disconnected ice fragments of various sizes, or of jumbled accumulations of fragments that have been pushed together and refrozen. The surface of the ice usually has a snow cover.

An ice cover influences the reflection and propagation of acoustic waves from underwater explosions. It also tends to subdue, or suppress, any surface eruptions from shallow underwater explosions. Since there are various practical needs for breaking and penetrating ice covers, the relevant blasting technology is of interest.

## DEEP UNDERWATER EXPLOSIONS

### Shock Propagation

When a concentrated charge of high explosive is detonated far below the surface of deep water, the initial pressure is typically of order 1 to 10 GPa (or more); intense compression is transmitted to the surrounding water, causing a steep <u>shock wave</u> to propagate in a spherical pattern at very high speed. Very close to the source, the shock amplitude is high and the shock passage is very fast. Peak overpressure in the water can exceed 100 MPa, shock velocity can exceed 5 km/s (several times the acoustic velocity), and positive phase duration is typically well below 10 ms. The

amplitude and velocity of the shock wave decrease as radius increases, until the disturbance becomes an acoustic wave, with velocity independent of amplitude (≈ 1.45 km/s). This process is qualitatively similar to shock propagation in air. However, while air and water are both fluids, with no shear rigidity, they are very different in terms of compressibility.

The explosive also forms a bubble of gas and water vapor, which expands, pulsates and migrates over time periods which are very long compared with the times for shock passage. Initially, the bubble is small, with very high temperature and pressure, but as it expands against hydrostatic pressure, the temperature and pressure fall. About half of the total energy of the explosion goes into bubble expansion, with the other half going into propagation and dissipation of the shock.

At a given distance, or scaled distance, from an underwater explosion, the shock amplitude is a lot higher than it would be in air (Fig. 1). In the range of available data, commonly with scaled radius from 0.4 to 10 $m/kg^{1/3}$ (8 to 200 charge radii), the attenuation of peak overpressure $p_m$ with radius r is more gradual in water than it is in air. For TNT, $p_m$ is approximately proportional to $r^{-1.13}$ at moderately close range. Higher pressures measured very near charges of HBX-1* attenuate a little more rapidly, with $p_m$ approximately proportional to $r^{-1.37}$. For air blast at comparable distances, $p_m$ is approximately proportional to $r^{-2}$ (see Part I, Fig. 19).

The relation between shock pressure and radius can be scaled in accordance with Hopkinson, or cube root, procedures (see Part I). The attenuation curve can thus be represented by approximate relations of the form

$$p_m = A\left(\frac{r}{W^{1/3}}\right)^{-\alpha} \tag{1}$$

where A and $\alpha$ are positive constants. The scaled distance $(r/W^{1/3})$ is, in effect, dimensionless, since $W^{1/3}$ represents charge radius (see Part I). This relation obviously breaks down as r → 0, so limits of applicability have to be set. Table 1 gives values of A and $\alpha$ for several types of explosive, together with the ranges of applicability. At a scaled radius

---

*RDX, TNT and aluminum.
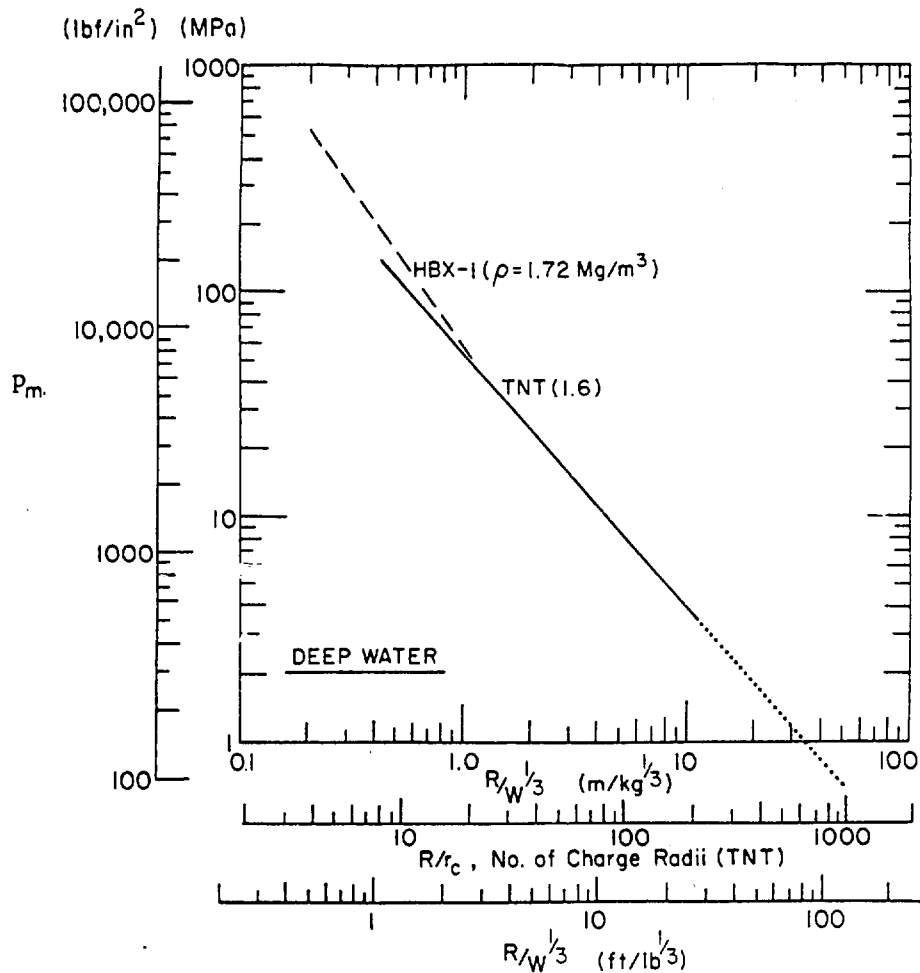
Figure 1. Attenuation of peak overpressure for spherical propagation from a concentrated high explosive source. Radius from the source is scaled with respect to: (a) the cube root of charge weight, (b) the charge radius. Data from Swisdak (1978).

of $1 \text{ m/kg}^{1/2}$, the variation of $p_m$ is given directly by the values of A. For underwater nuclear explosions, the values of A and $\alpha$ for TNT can be used if W is taken as 67% of the radiochemical yield (i.e., 1-kiloton yield is taken as $1.33 \times 10^6$ lb). For an acoustic wave, $\alpha \rightarrow 1.0$.

When using units of $\text{lbf/in.}^2$ ($p_m$), ft (r) and lb (W), the value of $\alpha$ is unchanged and the value of A is typically in the range $2.2 \times 10^4$ to $2.5 \times 10^4$. The SI value of A is multiplied by $145 \times (2.5208)^{\alpha}$.

Equation 1 applies to shock propagation in deep water, but it can also be used to estimate the incident shock at close range in shallow water as long as there is no interference by reflections from the water/air surface, from the bed of the water body, or from near-vertical walls.

3

Table 1. Attenuation constants for shock propagation in deep water. (Data from Swisdak 1978.)

| Explosive | Overpressure attenuation constants* | | Applicable range |
| | A | $\alpha$ | $p_m$ (MPa) |
|---|---|---|---|
| TNT | 52.4 | 1.13 | 3.4 – 138 |
| Pentolite | 56.5 | 1.14 | 3.4 – 138 |
| H-6 | 59.2 | 1.19 | 10.3 – 138 |
| HBX-1 | 56.7 | 1.15 | 3.4 – 60 |
| HBX-1 | 56.1 | 1.37 | 60 – 500 |
| HBX-3 | 50.3 | 1.14 | 3.4 – 60 |
| HBX-3 | 54.3 | 1.18 | 60 – 350 |

*Units such that $p_m$ is given in MPa when r is in metres and W is in kilograms.

## Variation of Shock Pressure with Time

In deep water, the pressure p behind a shock front decays with time t almost exponentially, although the tail of the wave actually has a small hump (Fig. 2). This secondary pulse is believed to be produced by reflections within the explosion source, brought about by the finite size and finite reaction time of the explosion. The positive phase duration at a given radius from the source can be characterized by a "relaxation time," or time constant, $\theta$, such that $\theta$ is the time taken for the shock pressure to decay to 1/e, or about 37% of the peak pressure $p_m$:
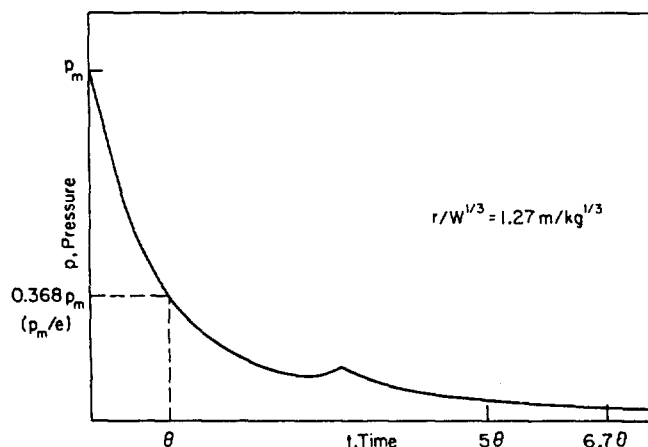


Figure 2. Pressure-time trace for an underwater shock passing a fixed point that is relatively close to the source. Pressure decay behind the shock front is approximately exponential, but there is a hump that is thought to be related to the finite size and finite reaction time of the explosion source. Following test data illustrated by Cole (1948).

4

Table 2. Scaling parameters for the relaxation time of a deepwater shock. (Data from Swisdak, 1978.)

| Explosive | Scaling constants for relaxation time* | | Applicable range |
| | B | β | $P_m$ (MPa) |
| --- | --- | --- | --- |
| TNT | 0.084 | 0.23 | 3.4 - 138 |
| Pentolite | 0.084 | 0.23 | 3.4 - 138 |
| H-6 | 0.088 | 0.28 | 10.3 - 138 |
| HBX-1 | 0.083 | 0.29 | 3.4 - 60 |
| HBX-1 | 0.088 | 0.36 | 60 - 500 |
| HBX-3 | 0.091 | 0.22 | 3.4 - 60 |

*Units are such that $\theta/W^{1/3}$ is given in ms/kg$^{1/3}$ when r is in metres and W is in kilograms.

$$p/p_m \approx e^{-t/\theta} \tag{2}$$

where t is the elapsed time since shock front arrival and $\theta$ is the relaxation time, or time constant.

The "time constant" is actually not constant; it varies somewhat with radius r from the source. By invoking similitude principles, $\theta$ can be scaled and its relation to r can be expressed as

$$\theta/W^{1/3} = B \, (r/W^{1/3})^{\beta} \tag{3}$$

where W is charge weight and B and β are positive constants, valid only within certain limits of applicability. Table 2 gives values of B and β
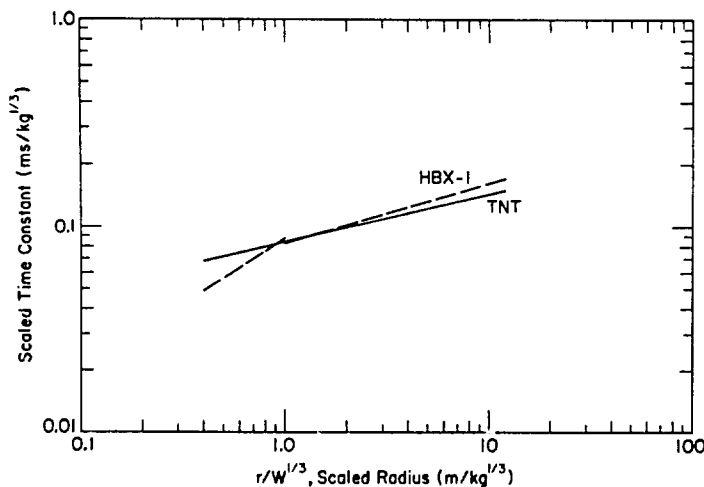


Figure 3. Variation of time constant, or relaxation time, with radius for deep underwater explosions of TNT and HBX-1. From equations given by Swisdak (1978).

5

for various explosives and for specified pressure ranges. For an acoustic pulse, $\beta \to 0$. Figure 3 shows the relation between $\theta/W^{1/3}$ and $r/W^{1/3}$ in graphical form for two explosives.

Equation 2 applies to shocks in deep water. When there is reflection from the water/air interface, from the bed of the water body, or from near-vertical walls, eq 2 applies to the incident shock only up to the time $t_c$ at which the reflected wave interferes with the tail of the incident wave (see later discussion of surface effects).

## The Impulse of a Shock in Deep Water

The impulse I of the shock wave (per unit area) is the integral of pressure p with respect to the time after shock arrival, t:

$$I = \int_0^{t_*} p \; dt$$

$$\approx \int_0^{t_*} p_m \, e^{-t/\theta} \; dt \; . \tag{4}$$

The limit of integration is typically taken with $t_*$ in the range $5\theta$ to $7\theta$. From similitude considerations, I can be scaled with respect to $W^{1/3}$, and the variation of the scaled impulse $I/W^{1/3}$ with the scaled radius $r/W^{1/3}$ can be expressed as

$$I/W^{1/3} = C(r/W^{1/3})^{-\gamma} \tag{5}$$

where C and $\gamma$ are positive constants for specified ranges of pressure or scaled radius. With the integration in eq 4 taken to $t_* = 5\theta$, values of C and $\gamma$ for various explosives are as shown in Table 3. For an acoustic pulse, $\gamma \to 1.0$. Figure 4 shows the relation between $I/W^{1/3}$ and $r/W^{1/3}$ graphically for two explosives.

Equation 5 applies in deep water where there are no shock reflections. At shallow depths, where the tail of the incident shock is truncated by a tensile wave reflecting from the surface (see Fig. 12 later), the impulse is reduced because the integration in eq 4 must terminate at the time of the surface cutoff.

6

Table 3. Attenuation constants for the impulse of a deep water shock. (Data from Swisdak, 1978.)

| Explosive | Attenuation constants for positive impulse* | | Applicable range |
|---|---|---|---|
| | C | $\gamma$ | $P_m$ (MPa) |
| TNT | 5.75 | 0.89 | 3.4 - 138 |
| Pentolite | 5.73 | 0.91 | 3.4 - 138 |
| H-6 | 6.58 | 0.91 | 10.3 - 138 |
| HBX-1 | 6.42 | 0.85 | 3.4 - 60 |
| HBX-1 | 6.15 | 0.95 | 60 - 500 |
| HBX-3 | 6.33 | 0.90 | 3.4 - 60 |
| HBX-3 | 6.70 | 0.80 | 60 - 350 |

*Units are such that $I/W^{1/3}$ is given in kPa-s/kg$^{1/3}$ (or MPa-ms/kg$^{1/3}$) when r is in metres and W is in kilograms. To convert kPa-s/kg$^{1/3}$ into $(lbf/in.^2)$-s/lb$^{1/3}$, multiply by 0.1114.
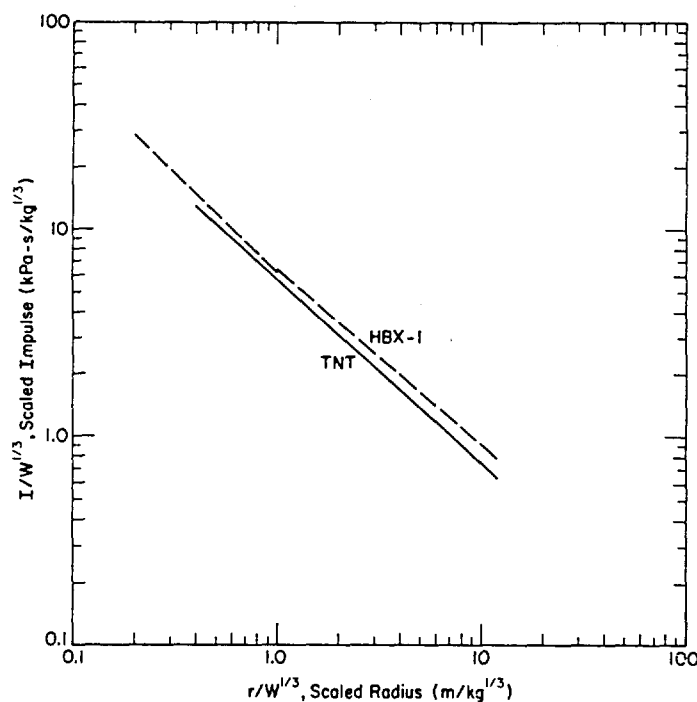


Figure 4. Attenuation of impulse with radius for deep underwater explosions of TNT and HBX-1. From equations given by Swisdak (1978).

7

## Refraction of Pressure Waves in Deep Water

For small explosions, shock propagation is almost spherical because the surrounding water is effectively homogeneous. However, for large explosions in deep water, the far-field effects are not those of simple spherical propagation. To appreciate the complications in deep water, it is convenient, and justifiable, to assume that the shock behaves as an acoustic wave, and also to think in terms of "ray paths," which are orthogonal to the wave front. In this way the wave can be treated by the ordinary laws of reflection and refraction, as developed in optics (see corresponding discussion for air blast in Part I).

In seawater, the acoustic velocity $c$ increases as temperature, pressure (or depth) and salinity increase (Fig. 5 and 6). Water density $\rho$ also varies with temperature, salinity and pressure, and the acoustic impedance $\rho c$ varies. Figure 7 indicates the variation of acoustic impedance with salinity and temperature at atmospheric pressure. In the ocean, where pressure increases with depth and where there are thermal and salinity stratifications, acoustic velocity varies appreciably with depth, and the depth profile of velocity changes from place to place and from season to season. In the topmost layers, the velocity profile can change diurnally.

If water conditions above an explosion are such that velocity increases with height above the charge, the "rays" are refracted in the sense that
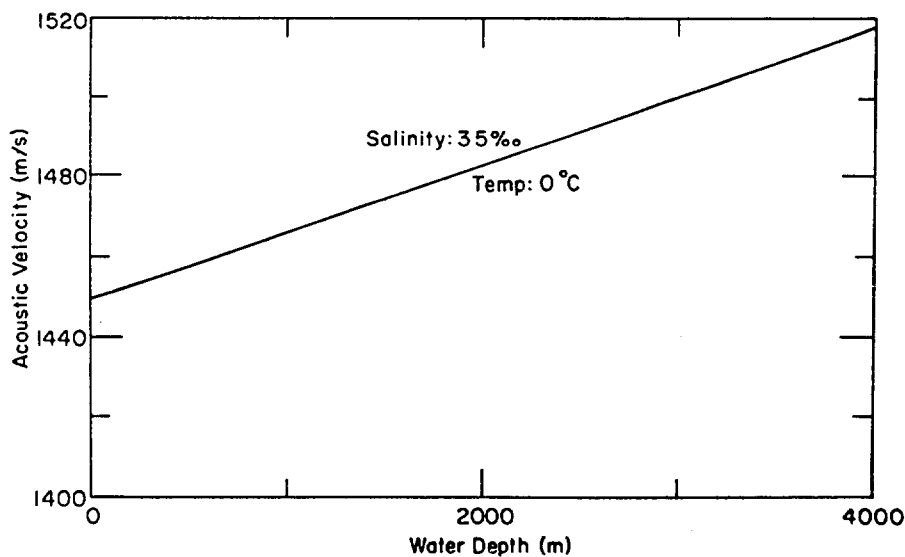


Figure 5. Variation of acoustic velocity with water depth for normal seawater at 0°C. Data from sound speed tables based on the Bradley-Wilson equation.

8
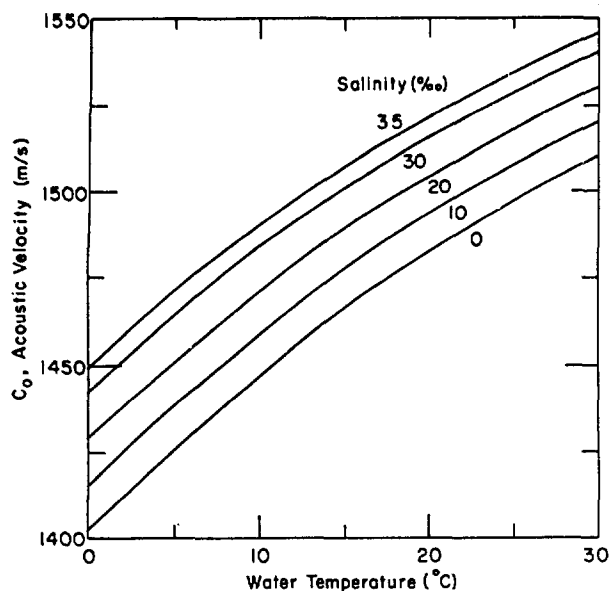
Figure 6. Variation of acoustic velocity with water temperature and salinity at atmospheric pressure. Data from sound speed tables based on the Bradley-Wilson equation.
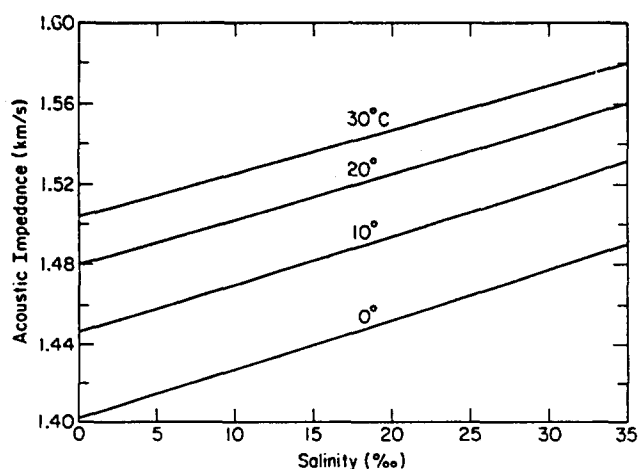


Figure 7. Variation of acoustic impedance with salinity and temperature at atmospheric pressure. The units of impedance are equivalent to specific gravity (dimensionless) multiplied by acoustic velocity in km/s.

they are bent downward (Fig. 8a). At sufficient distance from the source, the rays in a particular direction turn back into a downward direction, but if a ray reaches the surface before this happens, it undergoes regular surface reflection. At the radial limit of surface reflection, the refraction phenomenon creates a shadow zone which is not traversed by the pressure wave.

If the velocity profile has an inversion (Fig. 8b), refraction above and below the inversion occurs in opposite senses, again tending to create a shadow zone.

When the velocity gradient is small in the uppermost water layers, and also in the layers near the charge depth (Fig. 8c), some rays can turn around and cross the rays which start further from the vertical. This

9

again creates a sort of shadow zone, bounded at the bottom by the caustic, a surface which is the locus of crossover points.

If velocity increases both above and below the charge depth (charge near the minimum of a velocity profile), refraction above and below confines much of the energy to propagation within a horizontal layer, or "sound channel" (Fig. 8d).
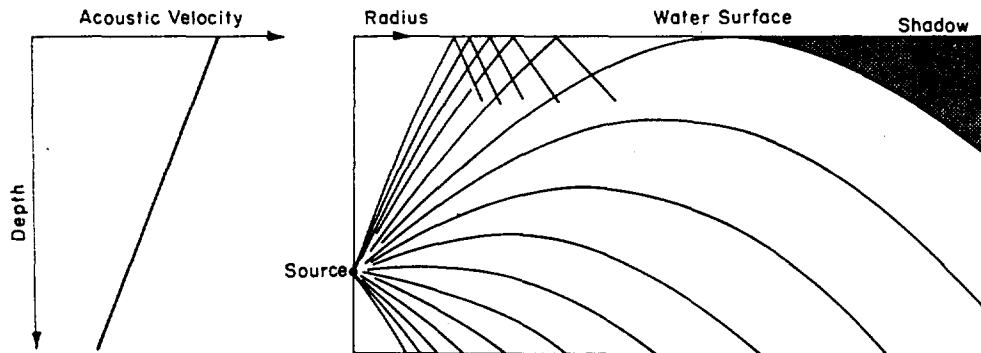
a. Velocity decreasing linearly with increasing depth.
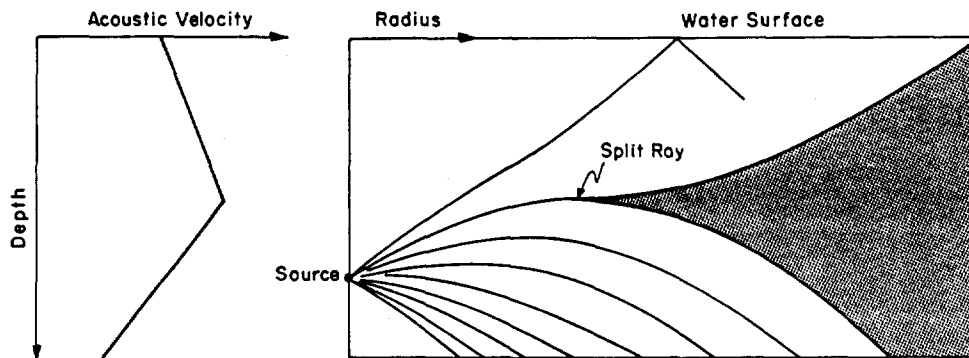
b. Velocity increasing linearly with depth below the surface, then decreasing linearly with depth below an inversion level.
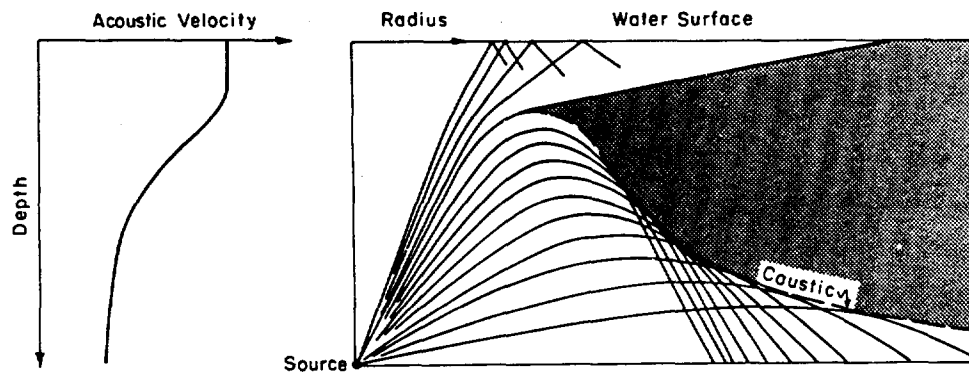
c. Velocity almost uniform in the uppermost water layers, with nonlinear decrease of velocity at greater depths.

Figure 8. Effects of acoustic velocity profiles on the propagation and refraction of pressure waves.

10
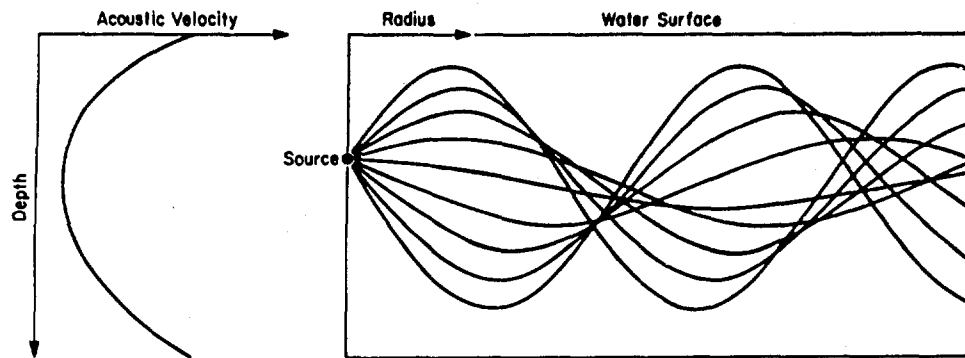
d. Velocity increasing above and below the source depth, form-
ing a "duct," or "sound channel."

Figure 8 (cont'd). Effects of acoustic velocity profiles on the
propagation and refraction of pressure waves.


## Bubble Expansion and Pulsation

The high temperature and pressure of an explosion form a gas bubble,
which initially has very great energy in very small volume. Transmission
of shock from the gas bubble to the water depletes the energy of the bubble
and lowers the internal pressure somewhat, but the gases continue to expand
rapidly, forcing the surrounding water to flow radially outward against
hydrostatic pressure, aided somewhat by after-flow from the shock passage.
During expansion to ambient hydrostatic pressure, the radial flow of water
accelerates. The inertia of the radial water flow allows the bubble to
over-expand, so that its internal gas pressure eventually drops below the
local hydrostatic pressure while the radial flow is decelerating to zero
velocity. At this stage the water flow reverses and the bubble starts to
collapse. Inertia allows the bubble to over-compress, and the collapse
motion becomes very fast (of order 60 m/s) just before it is halted by gas
compression. The abrupt arrest of bubble collapse creates in the surround-
ing water a pressure pulse which is significant, but much smaller than the
initial shock (see Fig. 16). By contrast, at maximum bubble expansion
there is very little energy transmitted to the water because the expansion
phase ends more gradually. The bubble pulsation is damped by energy losses
resulting from acoustic emission in the secondary pressure pulses and also
from turbulence. Thus, in very deep water, the pulsation should eventually
cease.

11

The behavior of the bubble from a nuclear explosion is similar, but there are significant differences. The bubble from high explosives contains mainly gaseous explosion products from the charge itself; these have constant mass, and the charge has finite size. The bubble from a nuclear explosion, which has temperatures and pressures very much higher than those of HE detonations, is formed by vaporization, dissociation and ionization of water as shock energy is dissipated. The nuclear "charge" is essentially a point source. Later in the bubble development, condensation can reduce the mass of vapor in the nuclear bubble, producing bubble pulse energy losses that are greater than corresponding losses for HE bubbles.

During the first bubble pulse of a chemical explosive, the maximum bubble radius $R_{bm}$ and the period of the oscillation $T_1$ vary with the charge size and the charge depth. The influence of charge size can be dealt with by applying cube root scaling, defining a scaled bubble radius $\overline{R}_{bm}$ and a scaled period $\overline{T}_1$ such that

$$\overline{R}_{bm} = R_{bm}/W^{1/3} \qquad (6)$$

$$\overline{T}_1 = T_1/W^{1/3} \; . \qquad (7)$$

Scaled values of maximum bubble radius and bubble period are then inversely proportional to powers of the absolute hydrostatic pressure, or total head. If the pressure, or head, is expressed in metres of water, the total head is $(H + H_0) \approx (H+10)$, where $H$ is charge depth and $H_0$ is atmospheric head, approximately equal to 10 m. The radius and period relations are:

$$\overline{R}_{bm} = \frac{R_{bm}}{W^{1/3}} = \frac{k_1}{(H+H_0)^{1/3}} \approx \frac{k_1}{(H+10)^{1/3}} \qquad (8)$$

$$\overline{T}_1 = \frac{T_1}{W^{1/3}} = \frac{k_2}{(H+H_0)^{5/6}} \approx \frac{k_2}{(H+10)^{5/6}} \qquad (9)$$

where $k_1$ and $k_2$ are constants for a given explosive. Table 4 gives values of $k_1$ and $k_2$ for several explosives, and the effect of charge depth is illustrated in Figure 9. The ratio $k_2/k_1$ does not vary much from one explosive to another. Bubble period is relatively easy to measure, so

Table 4. Parameters for the first bubble pulse. (Data from Swisdak, 1978.)

| Explosive | Radius constant $k_1$ | Period constant $k_2$ | $k_2/k_1$ |
|-----------|-----------------------|-----------------------|-----------|
| TNT | 3.50 | 2.11 | 0.603 |
| Pentolite | 3.52 | 2.11 | 0.600 |
| HBX-1 | 3.95 | 2.41 | 0.610 |
| HBX-3 | 4.27 | 2.63 | 0.616 |
| H-6 | 4.09 | 2.52 | 0.616 |

Units of $k_1$ and $k_2$ are such that radius is given in metres and time is given in seconds when charge depth is in metres and charge weight is in kilograms.
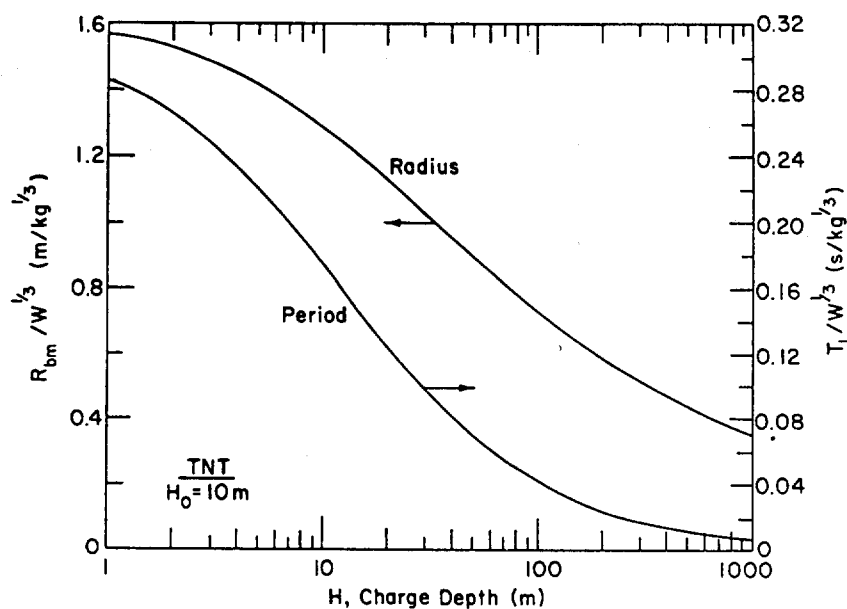


Figure 9. Variation of theoretical bubble radius and bubble period with charge depth. The curves are in accordance with eq 8 and eq 9, using the parameters for TNT given in Table 4.

relations involving T are useful for calculating other quantities, such as bubble depth or bubble energy (see eq 13-15 later). For comparison of nuclear and HE bubble effects, the "weight" of the nuclear charge W (TNT equivalent) is taken as about 84% of the radiochemical yield (usually expressed in kilotons, where 1 kt is equivalent to $10^{12}$ calories).

The period of the first bubble pulse, $T_1$, gives the time interval between the shock wave and the first pressure pulse formed by bubble collapse.

## Damping of Bubble Pulsations

When a bubble pulsates, the expansion and compression of the gas is effectively elastic, so that much of the internal energy is conserved. However, some energy is transferred irreversibly to the surrounding water and dissipated, partly by radiation of stress waves when the bubble collapse is arrested, partly by compression and turbulence in the water, and partly by breakup of the bubble surface into spray jets which cool the gas (Taylor instability).

Equation 9 gives, in essence, the period for the first bubble pulse as a function of detonation energy. A similar equation should be applicable to the nth pulse if the detonation energy is replaced by the residual energy $E_n$:

$$T_n = \frac{k(E_n)^{1/3}}{(H + H_0)^{5/6}} \tag{10}$$

where k is a constant. For successive bubble pulsations, the period T and the bubble energy E are then related by

$$\frac{T_{n+1}}{T_n} = \left(\frac{E_{n+1}}{E_n}\right)^{1/3} \left(\frac{H_n + H_o}{H_{n+1} + H_o}\right)^{5/6} \tag{11}$$

where $H_n$ and $H_{n+1}$ are the respective bubble depths for the two pulsations. If the rise of the bubble is slow relative to the bubble period, so that H is sensibly constant, then

$$\frac{T_{n+1}}{T_n} = \left(\frac{E_{n+1}}{E_n}\right)^{1/3} . \tag{12}$$

Some data given by Cole (1948) suggest that $(T_{n+1}/T_n)$ may be approximately constant during the first few cycles when the bubble is remote from free surfaces or rigid boundaries, with a value of about 0.77 (see Fig. 10a). This implies that $(E_{n+1}/E_n) \approx 0.46$, again approximately constant from one cycle to the next. This further implies an exponential decay of bubble energy with the number of cycles. Other test results discussed by

14
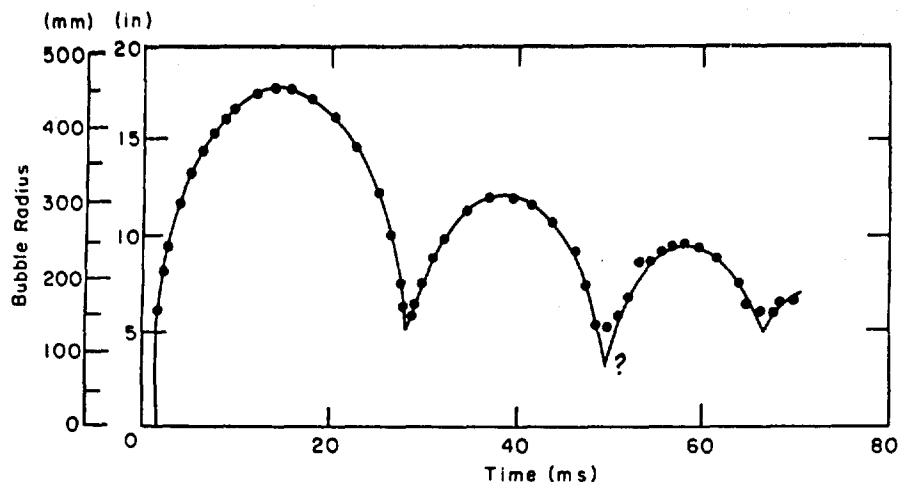
a. Radius plotted against time for three bubble pulses from a 0.25-kg charge of tetryl at 91 m depth. After Cole (1948).
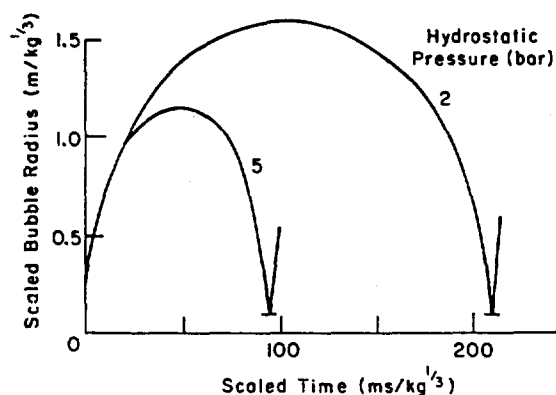


b. Calculated values of scaled radius plotted against scaled time for the first bubble pulse under ambient pressures of 2 and 5 bars. After Johansson and Persson (1970).

Figure 10. Variation of bubble radius with time for a high explosive charge in deep water.

Cole (1948) indicate a bigger energy loss in the first contraction, with $E_2/E_1 = 0.34$, but smaller relative loss in the second contraction, with $E_3/E_2 = 0.54$. For a non-migrating bubble, Snay (1957) gave $E_2/E_1 \approx 0.38$. If an explosion produces steam, it is to be expected that energy losses will be relatively high, with $E_{n+1}/E_n$ varying considerably from cycle to cycle (increasing with n if there is no migration).

When the bubble is rising rapidly, migration depletes the internal energy of the bubble.

Maximum bubble radius will also decay with pulse repetition. If equations similar in form to eq 8 and eq 9 are accepted for the nth pulsation, then

$$\left(R_{bm}\right)_n = \frac{k_1}{k_2} (H + H_0)^{1/2} T_n . \tag{13}$$

15

In other words, maximum bubble radius is directly proportional to the period, and it will tend to decrease by a fixed percentage (say about 23%) with each cycle. Figure 10a illustrates the fluctuation of radius with time in deep water, showing $R_{bm}$ for the second and third pulses as roughly 70% of the value for the preceding pulse in each case. Figure 10b shows scaled radius as a function of scaled time for the first bubble pulse under two different ambient pressures.

## Pressure Pulses from the Gas Bubble

Each collapse of a pulsating gas bubble produces a pressure pulse (see Fig. 16 later). When measured over a broad frequency band, the amplitude of the first bubble pulse is appreciably smaller than the amplitude of the shock wave, and at close range the pressure rise is comparatively slow. However, the duration of the bubble pressure pulse is quite long, so that the impulse (area under the pressure-time trace) is comparable to that of the shock. The bubble pulse propagates as an acoustic wave, with the wave front tending to steepen progressively ("shock-up" – Part I, Fig. 3).

Neither the absolute amplitude of the bubble pulse nor the amplitude relative to the initial shock can be predicted with confidence. The bubble pulse is affected by bubble migration, there may be interference by shock reflections from distant boundaries, the pulse shape can change during propagation, and there are slightly different attenuation rates for the shock and the bubble pulse.

For a deep explosion in very deep water, the peak pressure of the first bubble pulse, $p_{b1}$, varies with scaled radius $r/W^{1/3}$ as

$$p_{b1} = k \ (r/W^{1/3})^{-1} \tag{14}$$

where k is a coefficient which has a weak dependence on the total head (H + $H_o$). Swisdak (1978) used TNT data from Slifko (1967) and gave k = 9.03 when $p_{b1}$ is in MPa and $r/W^{1/3}$ is in m/kg$^{1/3}$. This value of k was for $152 < (H + H_o) < 1219$ metres, and $79 < (r/W^{1/3}) < 5500$ m/kg$^{1/3}$. The corresponding relation for the peak shock pressure $p_m$ was eq 1 with A = 50.4 (i.e. 4% smaller than the TNT "close range" value in Table 1), and $\alpha$ = 1.13. These relations for $p_m$ and $p_{b1}$ are shown graphically in Figure 11. At the closest applicable range, $p_{b1}/p_m$ = 0.315; at the most distant applicable range, $p_{b1}/p_m$ = 0.548.
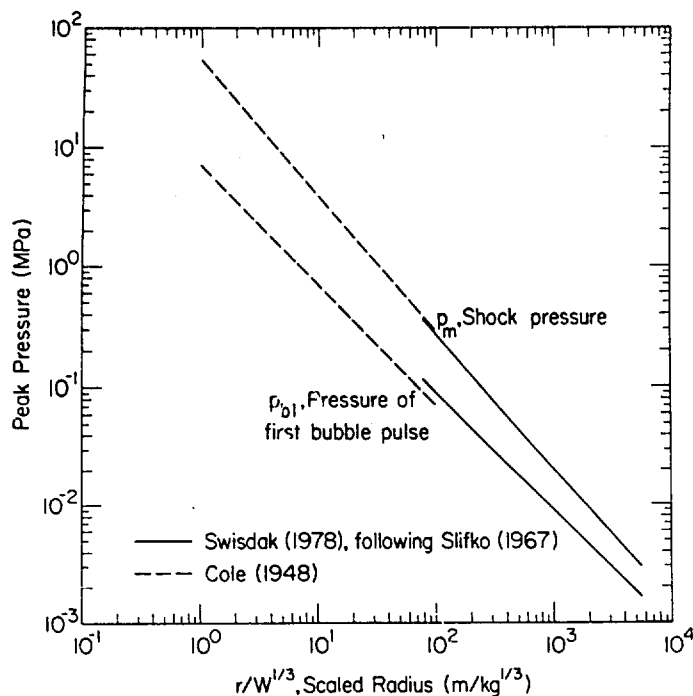
Figure 11. Approximate magnitude of bubble pulse amplitude for the first collapse of a non-migrating bubble in deep water. The peak shock pressure is plotted for comparison. The full lines are relations for TNT given by Swisdak (1978) and credited to Slifko (1967). The dashed lines are relations given by Cole (1948).

Cole (1948) stated that "The peak pressure in the first bubble pulse is no more than ten to twenty percent of that of the shock wave ...". Cole's example of bubble pulse data for a scaled radius of 3.6 m/kg$^{1/3}$ (Cole's Fig. 1.5 and Table 9.2) gives $p_{bl}/p_m$ = 0.045. Cole's example implies that k ≈ 1.96 in eq 14, so that the relative amplitude of the bubble pulse at distant ranges is a good deal lower than that indicated by Swisdak's equations. However, a theoretical relation given by Cole (his eq 9.13) converts to give k = 7.08, which yields values of $p_{bl}$ only 22% lower than those given by Swisdak's equation. Cole's relations seem to be developed for application at relatively close range, and they have been plotted accordingly in Figure 11.

## Bubble Rise

Being buoyant, the gas bubble rises towards the surface while it is expanding or pulsating. However, the characteristics of the motion seem rather strange at first sight.

A simple bubble from a non-explosive source rises in water, or any other liquid, much like a balloon, increasing in size as depth decreases, without pulsation. The speed increases as bubble size increases, maintaining a Froude number (based on equivalent bubble radius) that is very close to unity. It might therefore be expected that a pulsating bubble would rise quickly when in an expanded state, and slowly when highly compressed.

17

However, because the bubble size and bubble velocity are changing continuously, there are accelerations, and the instantaneous velocity lags behind the driving conditions. The top of the bubble moves farthest during expansion, and the bottom moves farthest during contraction. The result is that the upward motion tends to accelerate as the bubble expands, but maximum velocity of the bubble center is reached only when the bubble is collapsing again. The net result is that ascent of a spherical bubble in deep water is jerky, with maximum velocity when the bubble is small and minimum velocity when it is large, or just the opposite from what would be expected for steady motion. Displacement of the top or bottom of the bubble is the resultant of the rise motion and the radial pulsation. During collapse, the two components of motion are opposed at the top of the bubble, but they are additive at the bottom of the bubble.

Vertical migration becomes more pronounced as depth decreases, but at shallow depths the process of migration under gravity (buoyancy) is complicated by proximity to the free surface, as discussed later.

## UNDERWATER EXPLOSIONS NEAR THE SURFACE

### Shock Effects at the Surface

The shock wave propagating spherically from a shallow underwater explosion hits the surface and reflects as a tensile wave, or rarefaction wave. If the shock is weak when it reaches the surface, it can be regarded as an acoustic wave and the reflected wave can be imagined as emanating from a virtual source which is a mirror image of the true point of detonation. The shape of the incident wave behind the shock front will then be determined by the algebraic sum of the pressures from the incident wave and the reflected wave at any given instant. For strong shocks, however, this is an oversimplification.

The first contact of the shock wave with the surface is at a point vertically above the charge, and at this point there is normal reflection. The shock contact zone spreads out radially across the surface from this point, giving oblique reflections. In high-speed photographs taken from above, surface reflection of the shock wave creates a darkened "surface slick," a circular area that spreads extremely fast near surface zero, in accordance with arrival times for the shock. Spreading velocity for the slick, $dr_s/dt$, can be written as $U(d/r_s)(1 + Ut/d)$, where $U$ is shock

18

velocity, d is charge depth, and t is the time for the slick to reach radius $r_s$. For $r_s \leq d$, $dr_s/dt > U$.

The reflected rarefaction wave can reduce the net water pressure below original ambient pressure if charge depth is not too great (Fig. 12), and when the negative overpressure drops sufficiently low (near the vapor pressure), cavitation occurs. There is a limit to negative amplitude in the reflected wave because of the limit to the tension that can be sustained by water. The combination of "bulking" from cavitation and droplet ejection from shock impact causes a spray dome to form at the surface (Fig. 13).



a. Idealized surface cutoff.

b. Real cutoff requiring finite time.
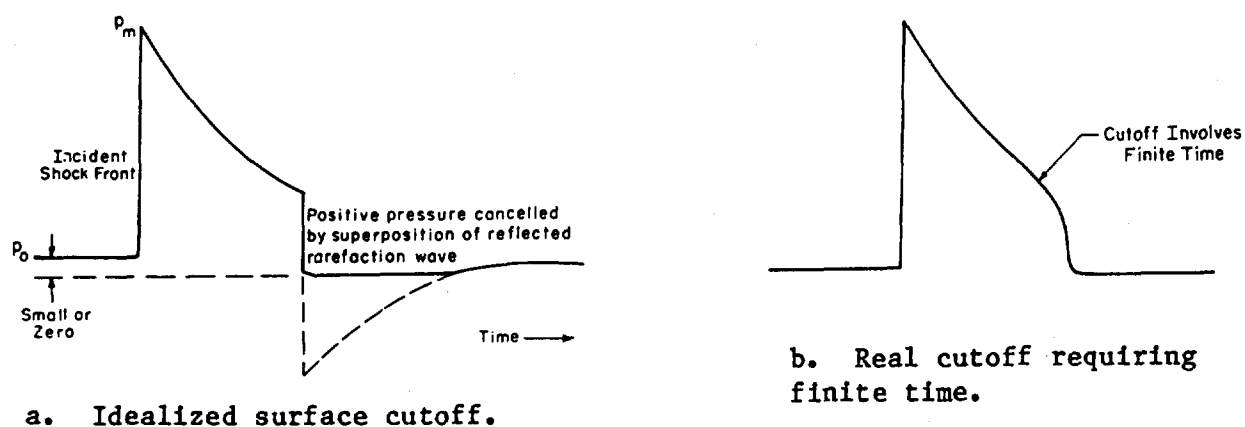
Figure 12. Effect of wave reflection from the water/air interface. The reflected rarefaction wave superimposed on the tail of the incident compressive wave can reduce the resultant pressure down to, or slightly below, the ambient hydrostatic pressure.
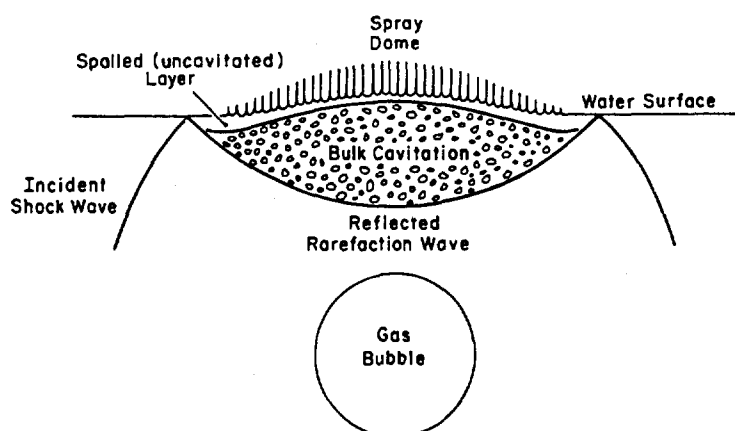


Figure 13. "Spalling" of the water surface by an underwater explosion (idealized). The incident compressive wave and the reflected rarefaction wave cause ejection of droplets and cavitation of surface layers. After Young (1973).

19

The spray dome, which is the first surface disturbance to appear, rises in a bell-shaped form, humped highest at the center because the initial velocity is proportional to the incident shock pressure. After a deep explosion, a secondary spray dome can be formed by the pressure pulse of the first bubble collapse, or by shock reflection from the bed.

The _initial_ upward velocity u of the surface water particles results from the shock reflection, with doubling of particle velocity. It can be expressed in terms of the incident shock pressure $p_m$ as

$$u \approx \frac{2\, p_m \cos\beta}{\rho_0 U} \tag{15}$$

where $\beta = \tan^{-1}(r_s/d)$, in which d is charge depth and $r_s$ is the horizontal radius from "surface zero" to the point considered. U is shock velocity ($\approx c_0$, the acoustic velocity in water) and $\rho_0$ is water density. If shock attenuation for all but the shallowest explosions is taken as a power relation, in accordance with eq 1, the variation of u with surface radius $r_s$ can be expressed as

$$\frac{u_r}{u_0} = \left(1 + (r_s/d)^2\right)^{-\frac{\alpha+1}{2}} \tag{16}$$

where $u_r$ is initial vertical velocity at surface radius $r_s$, $u_0$ is initial vertical velocity at "surface zero," and $\alpha$ is the attenuation constant from eq 1. Equation 16 defines the initial shape of the spray dome and shows how it is affected by charge depth. Since $\alpha \approx 1$, the exponent in eq 16 is approximately $-1$.

The interference of the reflected wave with the incident wave is called the _surface cutoff_. The abrupt cutoff of positive pressure shown in Figure 12a is an idealization; in reality, the cutoff takes a finite time (Fig. 12b) because the reflected wave is traveling through water disturbed by the incident wave. The difference between the arrival time of the incident shock and the reflected wave is called the _surface cutoff time_, $t_c$. It is given with sufficient accuracy by an acoustic approximation:

$$t_c \approx (1/c)\left[r_s^2 + (d_c + d_g)^2\right]^{1/2} - r/c \tag{17}$$

$$\approx (1/c)\left[r^2 + 4\, d_c d_g\right]^{1/2} - r/c$$
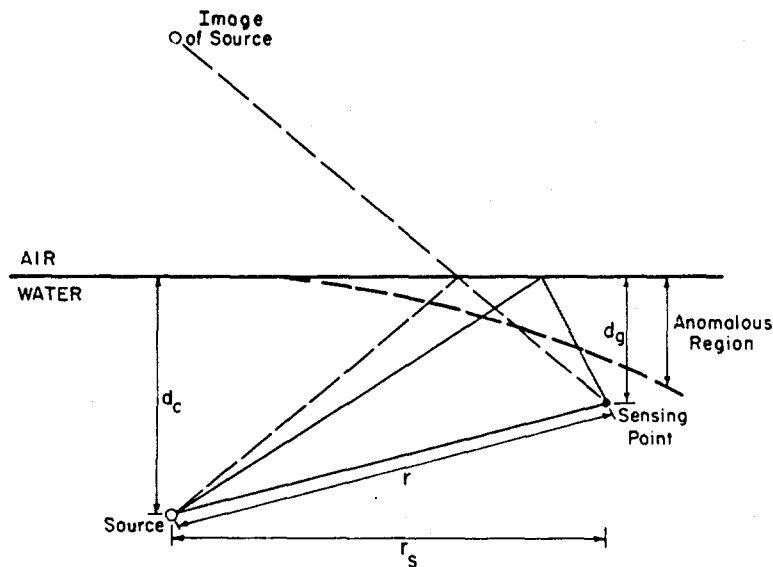
Figure 14. Reflections and interference of shock
waves at the water/air interface.

where c is acoustic velocity (strictly the shock velocity), $r_s$ is hori-
zontal distance from the charge to the sensing point, r is slant radius
from charge to sensing point, $d_c$ is charge depth, and $d_g$ is depth of
the sensing point (Fig. 14). Values of $c_0$ at atmospheric pressure are
given in Figure 6, with depth effects on $c_0$ shown in Figure 5.

As $d_g$ decreases, so $t_c$ decreases and eventually (because the
reflected wave travels in shocked water) the reflected wave interferes with
the shock front itself, reducing the amplitude of the shock front. This is
analogous to Mach stem formation in an air blast over a solid surface, but
in the case of underwater shock the fused shock fronts reduce the amplitude
instead of magnifying it. The zone within which the peak overpressure is
reduced by the reflected wave is called the anomalous region (Fig. 14).

In a "contact burst," where the charge is at the surface with half its
volume in air and half its volume in water, the distribution of shock pres-
sure in the water is strongly "anomalous." Figure 15 shows how peak over-
pressure varies with the depth of the sensor and with the radial distance
of the sensor from the charge. At any given radial distance from the
charge, shock pressure increases with increasing depth.

Bubble Motion Near the Surface

A bubble pulsating at great depth displaces the water radially, the
radial velocities decaying with distance from the bubble center. The

21
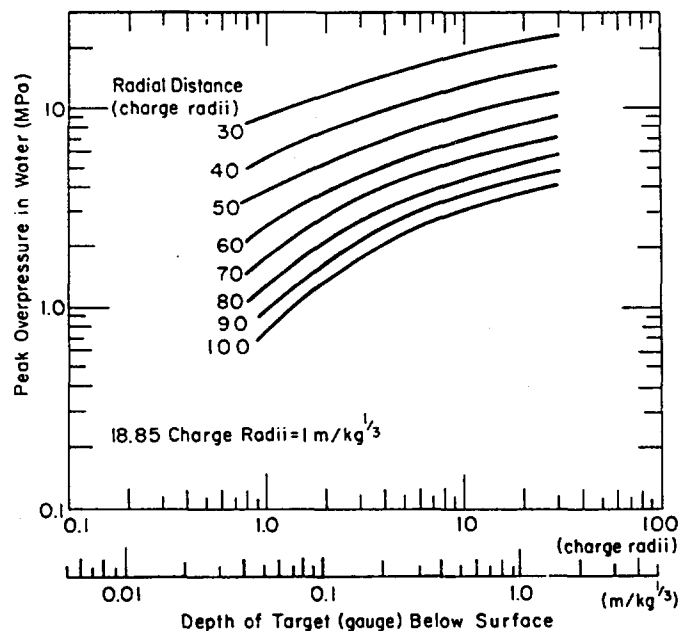
a. Peak overpressure as a function of scaled target depth, with scaled target radius as parameter.
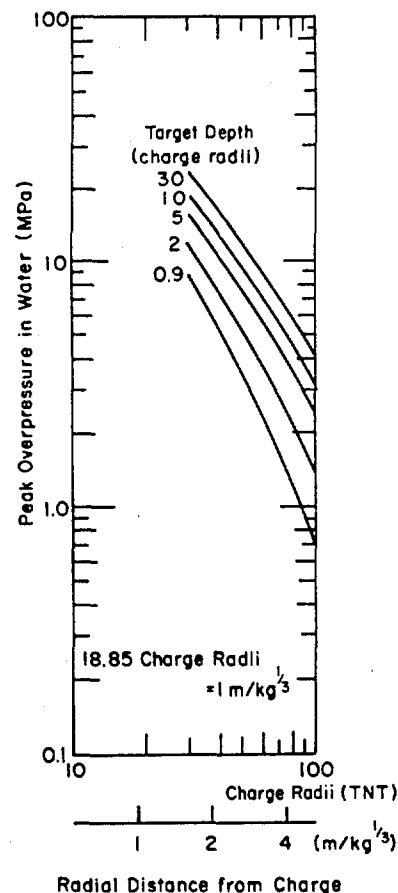
b. Peak overpressure as a function of scaled target radius, with scaled target depth as parameter.

Figure 15. Peak overpressures in water from an explosion at the air/water interface. Data from Swisdak (1978).

bubble period is relatively short at great depth, so that buoyancy effects are not very important to the pulsation. By contrast, the radial symmetry of the bubble motion is disturbed when a free surface or a rigid surface intersects the flow field; the period increases near the air/water surface, and buoyancy effects become significant there. The external pressure on the free surface (atmospheric) is constant, and therefore displacements of the water surface adjust so as to equilibrate the pressure. For a continuous rigid boundary (e.g. sea bed), flow must be parallel to the boundary.

During bubble expansion, water being displaced towards the free surface encounters less inertial resistance. During contraction, the relatively small mass of water above the bubble accelerates more rapidly than

22

the water below. Also, the pressure gradient relative to the mean pressure becomes more significant as depth decreases. Because of these things, proximity to the air/water interface affects the bubble pulsation, the bubble shape, and the rate of rise.

At maximum expansion the bubble is almost spherical, but during collapse the shape becomes distorted by hydrostatic pressure differences and by buoyant migration of the bubble. The bottom of the bubble, where hydrostatic pressure is greatest, moves inward more than other parts of the bubble surface. The effect is first to flatten the bubble from its expanded spherical shape, then to bulge the bottom inward like the base of a wine bottle. In cross section, the contracted bubble is kidney-shaped. This distortion can culminate in a collision between the bottom and top surfaces of the bubble; the bottom penetrates the top as a jet, leaving the bubble with a doughnut shape. As each collapse of the bubble is arrested, a pressure pulse is transmitted to the surrounding water (Fig. 16). Under certain circumstances, it is possible that the migrating bubble transforms into a vortex ring.
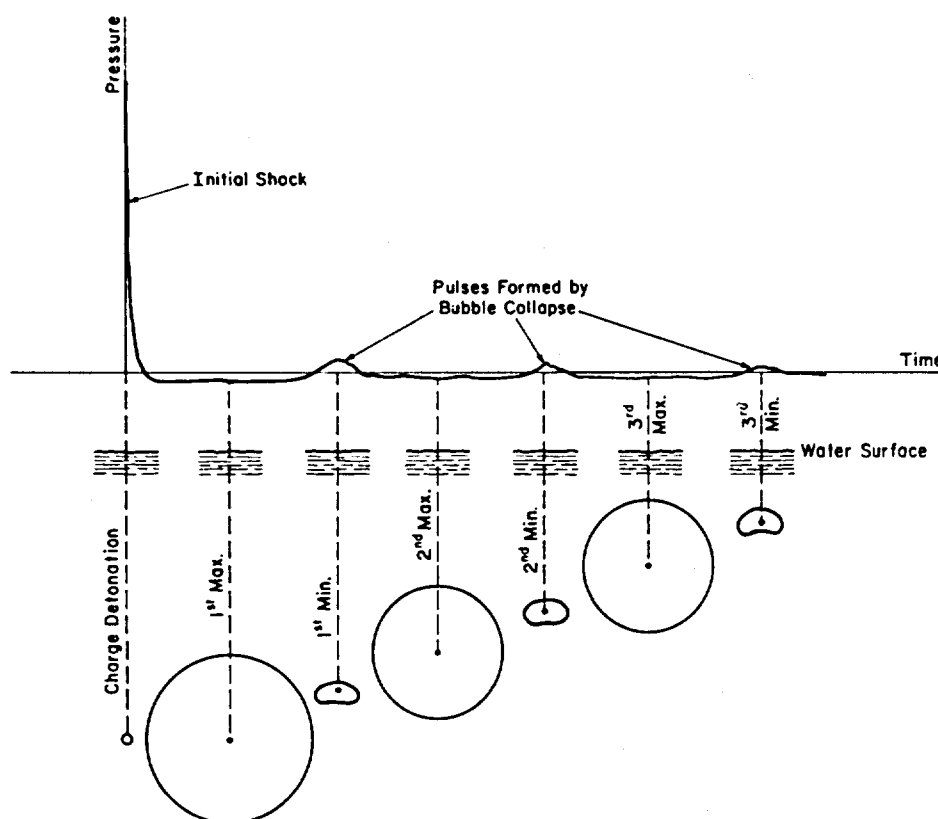


Figure 16. Secondary pressure pulses produced by successive collapses of the gas bubble during pulsation. After Snay (1957).

23
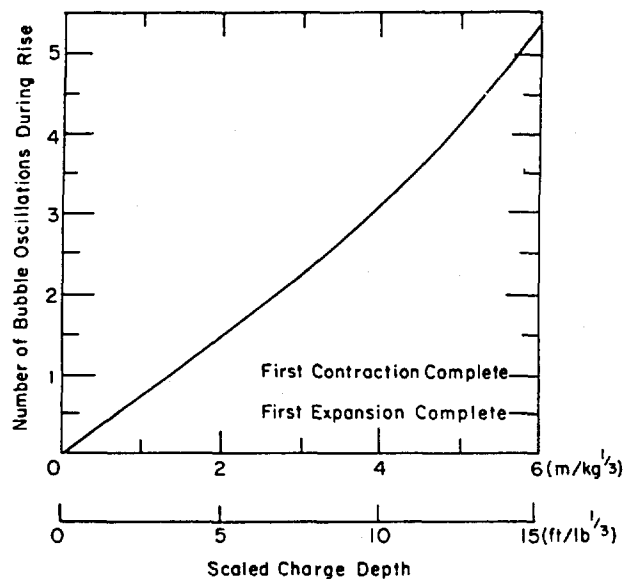
Figure 17. Number of bubble oscillations as a function of scaled charge depth for TNT charges in deep water. After Swisdak (1978).

Near the free surface, the bubble pulsates more rapidly and the period is shorter than it would be without the free surface. The theoretical period given by eq 9 can be adjusted to account for proximity to the surface or to the bottom of the water body (Cole 1948, Swisdak 1978), but the equations will not be reviewed here. An alternative to theoretical adjustment is to obtain effective values of $k_2$ in eq 9, using values of depth H and charge weight W that are of special interest. For example, one can plot $\ln(T_1/W^{1/3})$ against $\ln(H+H_0)$, fit a line that has a slope of -5/6, and thus obtain $k_2$.

During the collapse phase of bubble pulsation there is acceleration of the inward radial flow, and the flow downward from the free surface accelerates towards the bubble center at higher rates than flow from other directions. This gives the appearance of repulsion from the free surface, as the center of the bubble moves away from the surface.

The effect of the gas bubble when it reaches the surface will vary according to the number of pulsations it has undergone during its rise. Figure 17 gives the number of oscillations as a function of scaled charge depth. The graph also indicates the stage of bubble pulsation (expanding or contracting) at which the bubble reaches the surface.

24

## Surface Displacement by the Gas Bubble

When the gas bubble reaches the surface it produces an eruption of water, or of water and gas. If the scaled depth of the explosion is <u>very great</u>, there may be no visible effects at the surface, since the shock there is attenuated to practically nothing, the rising bubble has lost all its energy in multiple pulsations, and gases have been dissolved in the water. The depth at which all surface effects become completely suppressed is known as the <u>total containment depth</u>. As scaled charge depth <u>decreases</u>, the first noticeable surface disturbance may be a shock-induced spray dome, followed by bubble-induced upwelling, with water motion but no significant elevation of the surface. With further decrease of charge depth, there is a shock-induced spray dome and possibly a spray dome from the second pressure pulse (first bubble collapse). A mound of water is formed subsequently at the surface, with turbulent radial motion; this may develop into a hump of spray and foamy water. The mound is produced by the arrival of a bubble whose pulsations have been damped out during multiple oscillations. At still shallower depths, a ring of inclined plumes bursts through the dome of spray in a coronet pattern, throwing water radially outward to some extent. For <u>small</u> charge depths ($\leq 0.9$ $R_{bm}$, the so-called venting depth) the bubble reaches the surface level during its first expansion and the eruption develops in a columnar form. When the bubble expands through the surface plane, it does not necessarily vent directly and instantaneously to the atmosphere, since a layer of water is displaced upward. At charge depths slightly shallower than $0.9$ $R_{bm}$ the erupting gas is below ambient air pressure, and air is sucked into the eruption ("blow-in"). If a shallow explosion has sufficient depth for the bubble to develop and grow before it reaches surface level, the column of spray has a high speed vertical jet as its core in the later stages of development. When charges are just below the surface ($< 0.2$ $R_{bm}$), so that the gas bubble vents directly and positively ("blowout"), the water column is capped by a cloud of explosion products, or "smoke." Some typical features of surface eruptions are illustrated in Figure 18.

The characteristics of surface eruptions have been recorded for a range of charge depths and charge sizes, and boundaries for the various types of eruption have been defined by normalizing charge depth with
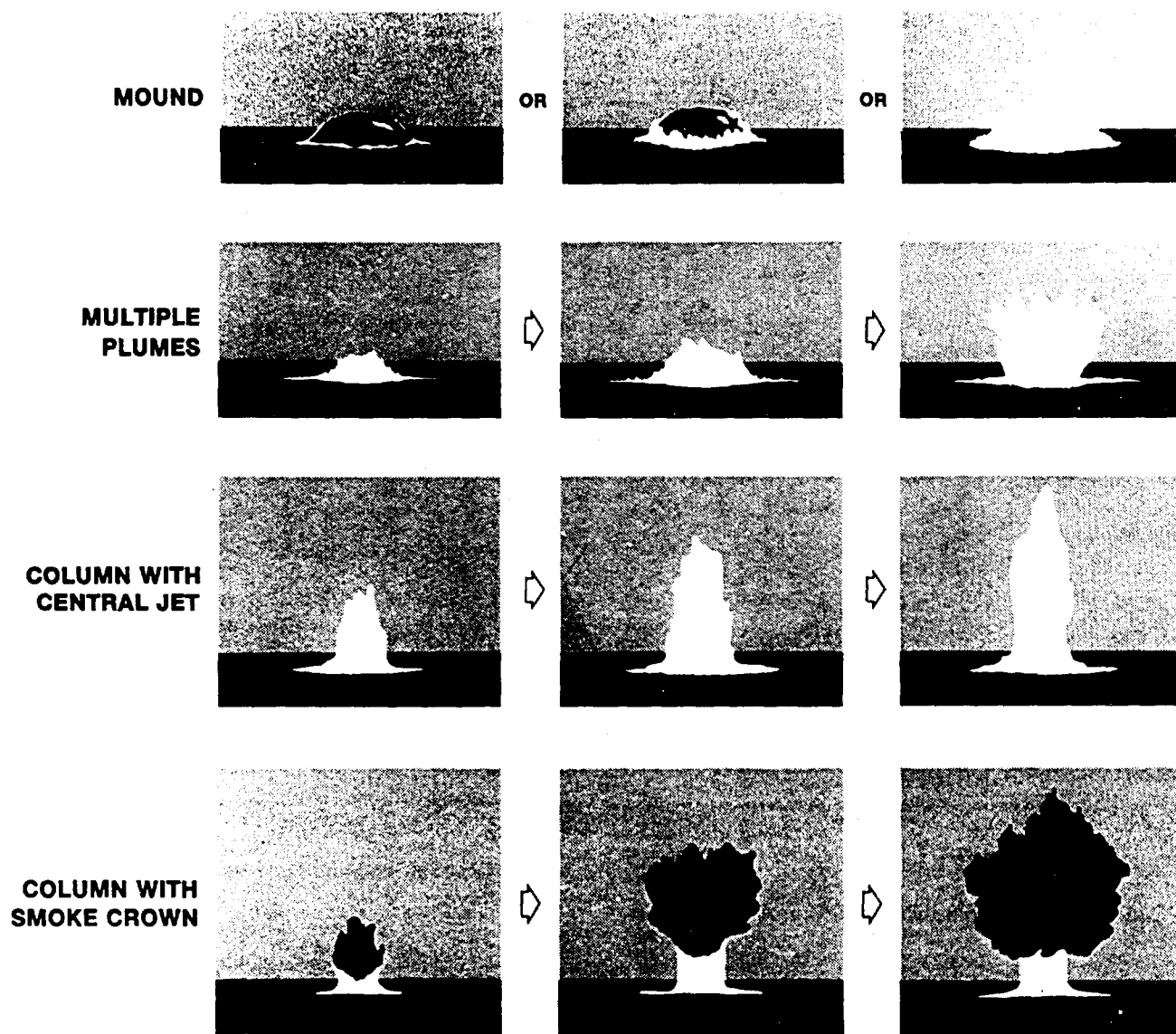
Figure 18.   Surface eruptions from underwater explosions.

respect to the theoretical maximum radius of the bubble during its first
pulse (Fig. 19).   The eruption behavior can be summarized as follows:

| Charge depth (bubble radii) | Type of surface eruption |
| --- | --- |
| > 40 | Total containment |
| 25-40 | Upwelling |
| 7-25 | Mounds |
| 4-7 | Mounds developing into plumes |
| 1-4 | Ring of plumes |
| 0.2-1 | Column with central jet |
| < 0.2 | Column with smoke crown |

26
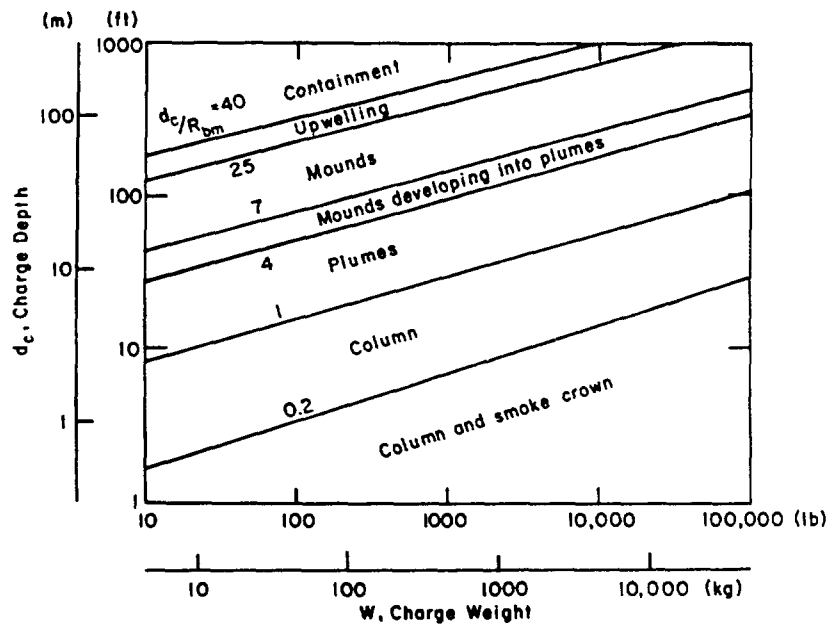
**Figure 19.** Surface effects from underwater explosions. After Young (1971).

For practical purposes it is useful to have scaled data expressed in terms of charge weight rather than bubble radius, but gravity effects complicate the scaling considerations. Ordinary cube root scaling is not directly applicable to charge depth where bubble effects are being considered. Bubble pressure is related to the total head $(H+H_0)$, rather than the water depth H, and bubble radius is a function of both charge weight and ambient pressure. In Figure 20 the depth $d_*$ which is equal to
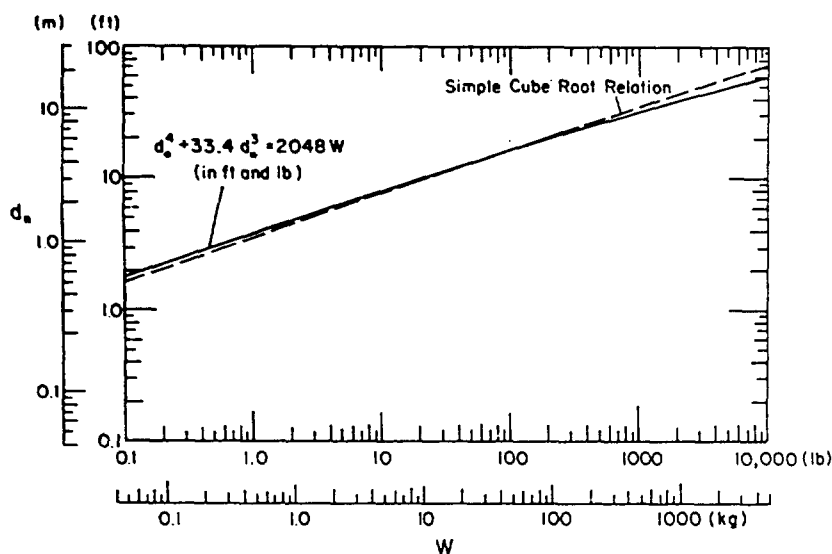


**Figure 20.** Critical charge depth $d_*$ plotted against charge weight W. $d_*$ is defined by $d_* = R_{bm}$, and the relation between $d_*$ and W is given by eq 8. The relation is compared with a simple cube root relation to show that, over a limited range of charge size, cube root scaling of charge depth provides a good approximation.

27

theoretical maximum bubble radius $R_{bm}$, i.e. $(d_*/R_{bm}) = 1$, is plotted against charge weight. The required relation is given by eq 8 after making the substitution $R_{bm} = H$, i.e.

$$H^4 + H_o H^3 = k_1 W. \qquad (18)$$

For the range of charge sizes shown on the graph, up to 5 tons (or 5 tonnes), a simple cube root relation provides a good approximation in the mid-range, and it can probably be accepted for charges weighing 1 to 1000 lb (0.5 to 500 kg). For very big charges, say over 1 ton (1 tonne), a better approximation is given by scaling with respect to the one-fourth root of charge weight. When the linear dimensions of surface eruptions are scaled with respect to the cube root of charge weight, without reference to charge depth, there is a tacit assumption that the scaled bubble radius $R_{bm}/W^{1/3}$ is independent of charge depth. Figure 21 shows that the actual variation of $R_{bm}/W^{1/3}$ is not very great for charge depths less than 10 m.

In Figure 22, part of Figure 19 has been replotted to show the effect of scaled charge depth on surface eruption when cube root scaling is em-
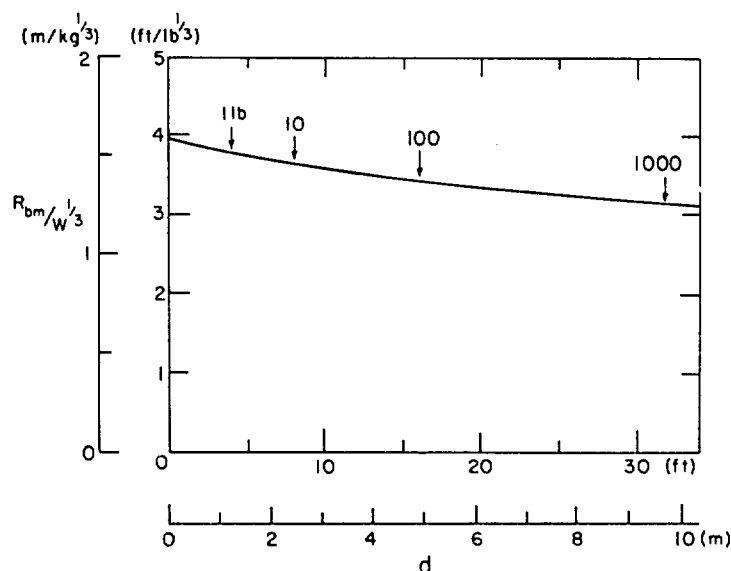


Figure 21. Scaled maximum bubble radius $R_{bm}/W^{1/3}$ plotted against absolute charge depth for TNT charges at depths up to 10 m. The arrows indicate the charge weights for which $R_{bm}$ is equal to the charge depth.
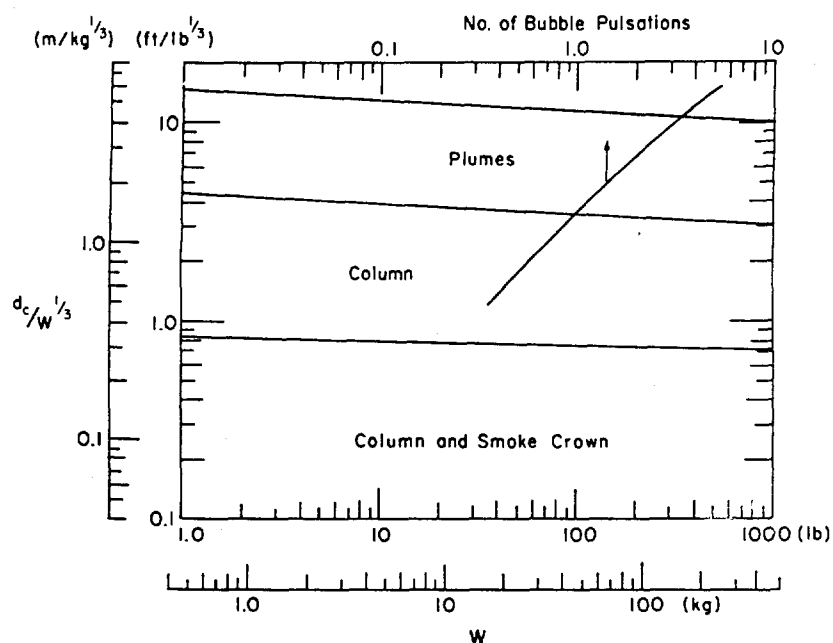
Figure 22. Part of Figure 19 replotted to give charge depth in terms of cube-root scaling. Data for bubble pulsations from Figure 17 have also been added.

ployed, and when the effects illustrated in Figures 20 and 21 are taken into account. The graph also shows the number of bubble pulsations according to Figure 17. Columnar waterspouts all occur during the first bubble pulse, but plume eruptions may occur at any stage of bubble pulsation during the second and third oscillations.

When the columnar types of waterspouts collapse and fall back, the falling spray forms an annular, or toroidal, cloud over the water surface. This ring of spray is then driven radially outward as a two-phase flow. The phenomenon is termed base surge.

## Dimensions and Ejection Velocities for Waterspouts

The scaled dimensions of the waterspout can vary in a complicated way, especially when there are multiple bubble pulsations before venting, but some predictions of dimensions can be made. The two characteristic dimensions for columnar waterspouts are diameter and maximum height.

For columnar discharges, several different diameters have been identified. The maximum diameter $D_{max}$ is the diameter of the well-defined visible column just above the base. Some investigators have also defined the diameter of an "effective column," which is a denser water column

29

Figure 23. Scaled diameter for waterspouts from
underwater explosions. The diameter of the gas
bubble at its first maximum is also plotted for
charge weights of 10 and 100 kg. Data for $D_{max}$
from Swisdak (1978).

inside the masking spray cloud that defines $D_{max}$. Finally, there is a
central core consisting of a high-speed jet, which is sometimes seen shoot-
ing out of the top of the column like a fountain.
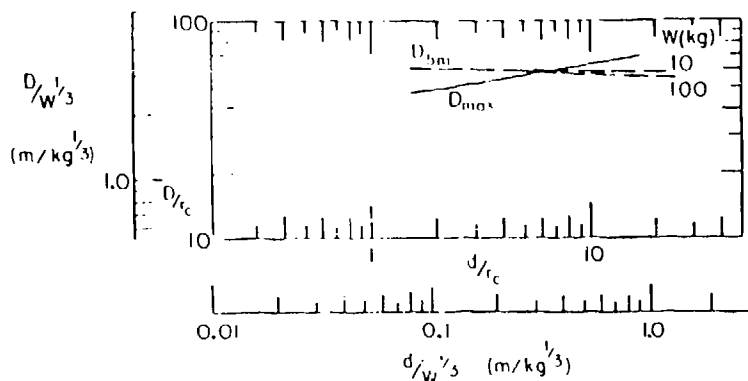
Figure 23 gives $D_{max}$ as a function of charge depth d, with dimen-
sions scaled with respect to charge radius, or to cube root of charge
weight. The data for $D_{max}$ (Swisdak 1978) are for charges lying on the
bed in shallow water, but they are believed to be applicable for charges at
the same depth in deep water. The relation for $D_{max}$ is

$$D_{max}/W^{1/3} = 3.71\left(d/W^{1/3}\right)^{0.166} \approx 3.71\left(d/W^{1/3}\right)^{1/6} \tag{19}$$

where the units of $D_{max}$ and d are metres and W is in kg. The limits of
applicability are $0.08 < (d/W^{1/3}) < 0.88$.

For explosions at greater scaled depths, where the surface eruption
forms more squat spray clouds, the maximum base diameter of the waterspout
has been expressed as a function of charge depth with different scaling
parameters. The waterspout base diameter $D_w$, measured as a maximum value
at surface level, is scaled with respect to the cube root of charge weight
as $D_w/W^{1/3}$. The charge depth d is scaled with respect to the fourth
root of charge weight as $d/W^{1/4}$. Data in this form (Swisdak 1978) were
plotted to obtain the envelope shown in Figure 24. The values of $D_w$ are
upper limit values intended to indicate "safe" distances.

The available data for height of the waterspout are all scaled such
that scaled height is in the form $H/W^{1/3}$ and scaled charge depth is in
the form $d/W^{1/4}$. Data for the maximum height of the column or jet from

30
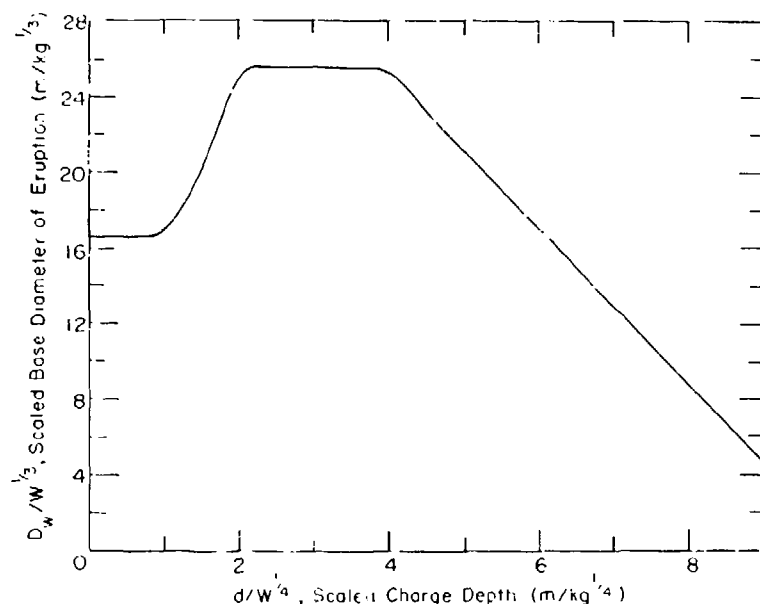
Figure 24. Upper limit of base diameter for sur-
face eruptions from underwater TNT explosions.
Data from Swisdak (1978).
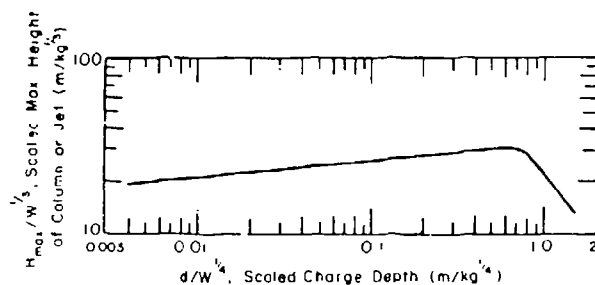


Figure 25. Maximum height of the col-
umn or jet formed by charges lying on
the bottom in shallow water. Data from
Swisdak (1978).

shallow explosions, $H_{max}$, are given in Figure 25. These results are for

charges set on the bottom, but it is thought that column height is much the

same when charges are suspended at the same depths in deep water (Swisdak

1978). The results for deeper charges in deep water (not on bottom) are

somewhat different, as shown in Figure 26, which gives upper limit values

for $H_{max}$ and compares this envelope with representative values from

Figure 25.

Columnar waterspouts emerge from the surface at high velocity, then

decelerate as they rise against resistance from gravity and air drag. The

first ejection of water occurs when the shock hits the surface, as des-

31
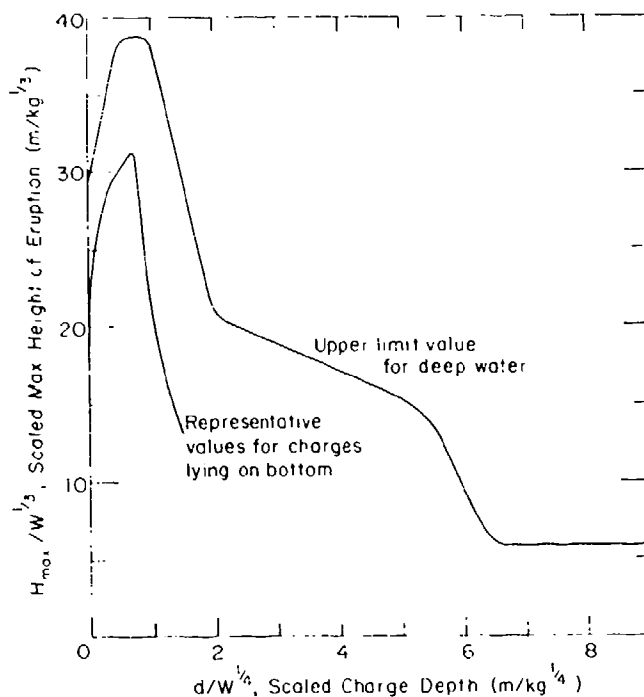
Figure 26. Height of eruptions produced by TNT charges set at various depths. The top curve is an upper limit envelope for charges suspended in deep water. The lower curve gives representative values for charges lying on the bottom, as in Figure 25. Data from Swisdak (1978).

cribed earlier. Initial ejection velocities are given by eq 15 and 16. The initial velocity $u_i$ for a point directly above the charge ("surface zero") can be expressed by substituting eq 1 into eq 15:

$$u_i = \frac{2A}{\rho_o U} \left(\frac{d}{W^{1/3}}\right)^{-\alpha} \tag{20}$$

where A and $\alpha$ are shock attenuation constants from Table 1, $(d/W^{1/3})$ is scaled charge depth, $\rho_o$ is water density and U is shock (or acoustic) velocity. For this relation to apply, $(d/W^{1/3})$ should be greater than about 0.4 $m/kg^{1/3}$, or $ft/lb^{1/3}$. For explosives such as TNT and Pentolite, the approximate magnitude of initial ejection velocity is $u_i \sim 70 \ (d/W^{1/3})^{-1.14}$ m/s when $(d/W^{1/3})$ is in $m/kg^{1/3}$.

Surface displacement by the gas bubble is more complicated, but it appears to give ejection velocities close to those predicted by eq 20. Figure 27 gives an impression of initial upward velocity as a function of

32
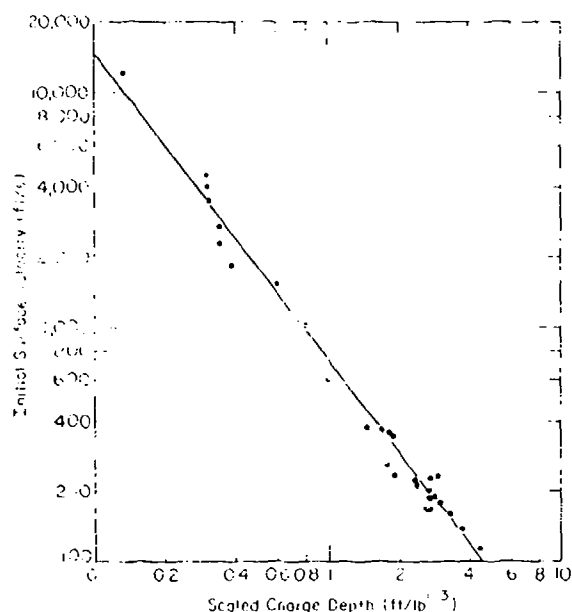
Figure 27. Initial vertical velocity as a columnar waterspout begins to burst through the water surface. Unscaled velocity is plotted against scaled charge depth. Based on test data compiled by Young (1973).

scale charge depth by combining various test results that were compiled by Young (1973). The trend of the limited data can be described by a power relation of the form

$$u_j = K(d/W^{1/3})^n \tag{21}$$

where K is a constant and n $\approx$ -4/3.

Ejection velocity for a given scaled charge depth is usually given in unscaled form, irrespective of charge size. However, the maximum height of the waterspout for a given scaled charge depth is commonly scaled with respect to $W^{1/3}$. If the maximum height of the waterspout is determined largely by gravity deceleration in accordance with elementary ballistic equations*, then for internal consistency the initial velocity ought to scale with respect to $(W^{1/3})^{1/2}$, or $W^{1/6}$.

Scaling with respect to the one-sixth root of charge weight has relatively little effect on the final result. For example, if a 50-kg charge is taken as the basis of comparison, then the scaling factors for 5-kg and 500-kg charges are, respectively, 0.68 and 1.46. Factors of this magnitude do not produce much displacement of data points which have been plotted on a logarithmic velocity scale.

---

* $v^2 = u^2 + 2fs$, where u and v are initial and final velocities respectively, f is acceleration, and s is distance traveled in the vector direction.

33

When a charge is detonated near the bottom, and far below the water
surface, the shock wave is reflected but some energy is absorbed by the
bottom material. If the bottom were completely rigid, and if the shock
behaved like an acoustic wave, there would be perfect regular reflection,
with no loss of energy in the reflection and a doubling of pressure at the
interface. With a charge in contact, the water around the charge would
experience effects equivalent to those produced in free water by a charge
twice as big (Cole 1948). Applying cube root scaling, th's would imply a
26% increase of peak overpressure (factor of $2^{1/3}$), a 59% increase of
impulse (factor of $2^{2/3}$), and a 100% increase of energy flux density*
(factor of 2). In reality, all bottom materials absorb energy and so the
predictions of simple theory are never fully met. Figure 28 gives some
results for the attenuation of energy flux density with distance along the
bed when the charge is lying on the bottom. The attenuation curve for free
water is compared with attenuation curves for charges lying on "hard
bottom" and on mud. Close to the charge, the hard bottom appears to give
an amplification of energy flux density which is well below the theoretical
factor of 2, but further away from the charge there is a doubling, as pre-
dicted by simple theory. In the case of charges lying on mud, the energy
flux along the bed is actually reduced below the values for free water.
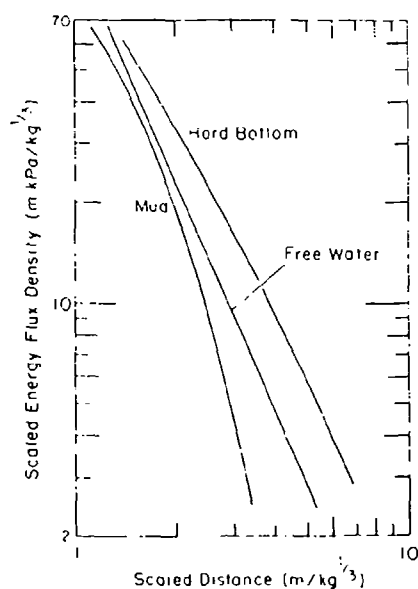


Figure 28. Effects of contact between the
charge and the bed for hard and soft bottom
materials. Scaled energy flux density in
the water is plotted against scaled distance
from the charge. After Swisdak (1978).

_____

* Energy per unit area (e.g. $N-m/m^2 \equiv Pa-m \equiv N/m$)

## Environmental Factors

As long as water remains in the liquid state, deep underwater explosions behave in much the same way, irrespective of whether the water is in the tropics or the polar regions. However, proximity to an ice surface introduces new considerations.

## Reflection and Refraction of Shock Waves

A weak shock propagating spherically from an underwater explosion reflects and refracts on contact with ice. From shock measurements made in water just below a uniform floating ice sheet, Barash (1966a) deduced the wave paths shown in Figure 29. The incident shock reflects from the lower surface of the ice and, subject to critical angle limitations, it also penetrates and refracts inside the ice. After refraction, part of the energy propagates along the ice/water interface and re-radiates back into the water. Another wave path reflects from the ice/air interface, returning through the ice and back into the water, with refraction. If the ice is very thick (iceberg or ice island), the ray shown as number 4 in Figure 29 will propagate and attenuate in the ice without significant reflection.

Figure 29. Ray paths for shock waves from an underwater explosion beneath an ice cover. After Barash (1966).

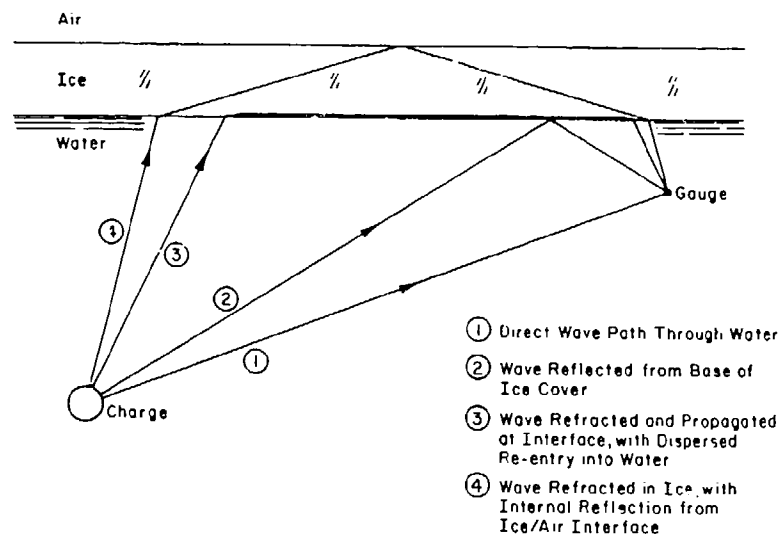If the shock amplitude is sufficiently high, the ice can deflect, fracture, shatter or deform.* This aspect of the material response is dealt with later.

## Cratering of Floating Ice By an Underwater Explosion

If an underwater explosion is big enough and shallow enough, it wi. burst through a surface ice layer to form a crater. The gas bubble dis- places the surface, discharging water, ice fragments and sometimes gaseous explosion products (Fig. 30). The final crater may have open water, or it may be completely choked with ice fragments.

A crater in floating ice is usually characterized only by its diameter or radius. The definition of crater diameter is arbitrary, and not always consistent for different studies. Crater diameter is the diameter of the zone where the ice is completely (and obviously) fractured, such that it is unable to sustain a bending movement. Additional radial and circumferen- tial cracks may extend beyond the crater without destroying the continuity and structural integrity of the ice sheet to a significant extent. The size of the crater depends on the size of the explosive charge, on the ice thickness, on the charge depth and, to a lesser degree, on the explosive type and ice type.

Available test data have been compiled and analyzed to provide design curves which give probable crater radius as a function of charge weight $W$, ice thickness $t$, and charge depth $d_c$ (Mellor 1972, 1982, 1986). For the limited range of the test data ($W < 300$ kg, $t < 4.3$ m), cube root scaling appears to be fully justified, so that all linear dimensions of the problem can be taken as proportional to $W^{1/3}$. Using scaled values for crater radius, ice thickness and charge depth, multiple regression analysis can be applied in order to derive the required prediction curves. Variations of explosive type and ice type seem to produce only second-order effects which cannot be evaluated from existing test data. However, some adjustment for explosive type can be made on the basis of the specific energy for each explosive (i.e. the heat of explosion) (Mellor 1982, 1986).

In practical ice-blasting work, it is convenient to refer charge depth to the base of the ice cover, and to have variables scaled with respect to

---

* "Spray reloading," which can occur by shock impact and cavitation behind thin air-backed plates (Snay 1957), is not expected to be significant in typical ice covers.

Figure 30. Eruption of a shallow-
depth charge (0.49 bubble radii)
through thin ice.
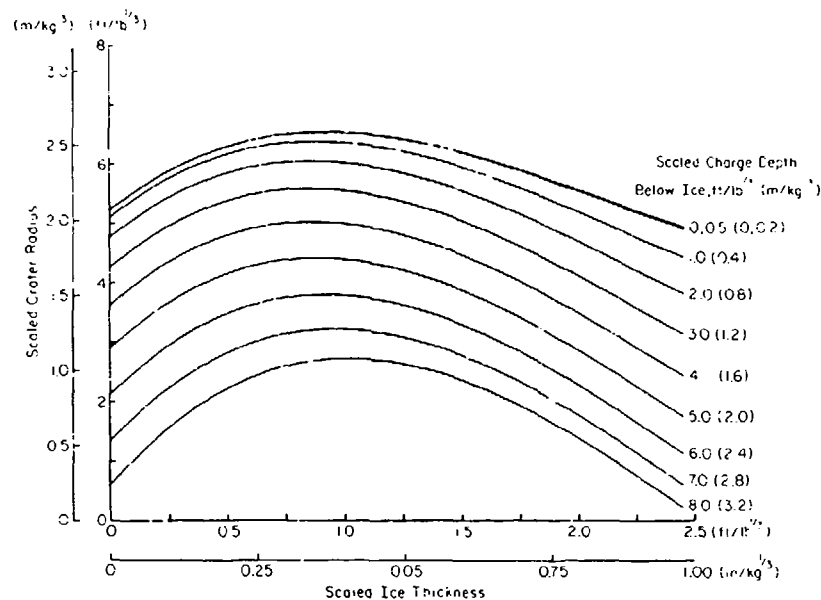
a. Scaled crater radius as a function of scaled ice thickness, with scaled charge depth as parameter.
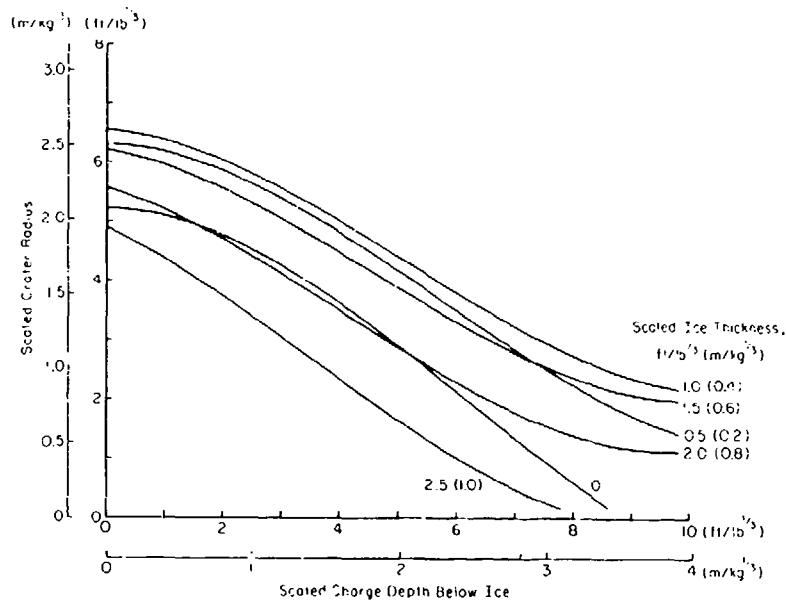


b. Scaled crater radius as a function of scaled charge depth, with scaled ice thickness as parameter.

Figure 31. Design curves for ice blasting.

38

the cube root of charge weight, as in Figure 31. However, when the governing physical principles are considered, it can be argued that: (1) the level of the water surface should be used as the datum for water depth, (2) linear dimensions should be scaled with respect to the theoretical maximum bubble radius. Consequently, available test data have been analyzed with: (a) cube-root scaling and water level as datum, (b) bubble-scaling and water level as datum. Results of the various regression analyses show that no practical advantages derive from these assumptions; the best empirical correlation is obtained with the assumptions used to produce Figure 31. Nevertheless, the results obtained with bubble-scaling (Fig. 32) provide some physical insight into the icebreaking process. The maximum attainable crater radius is about 1.63 times the maximum bubble radius, and it is achieved when the charge depth and the ice thickness are about 0.3 times the maximum bubble radius. This implies that water driven by the expanding gas from an optimum blast bursts through the ice during the first bubble expansion.

When the curves of Figure 31 are used to design a blast or to predict explosion effects, the usual input is a measured or estimated value of the ice thickness $t$. If the concern is with an optimum blast, the curves show that the biggest scaled crater is obtained when $t/W^{1/3} \approx 0.9$ ft/lb$^{1/3}$ (0.36 m/kg$^{1/3}$), so that optimum charge weight $W_{opt}$ is:

$$W_{opt} \approx 1.4\ t^3\ \text{lb} \qquad \text{with } t \text{ in feet}$$

$$(22)$$

$$W_{opt} \approx 21\ t^3\ \text{kg} \qquad \text{with } t \text{ in metres}$$

The best result is obtained with the charge almost in contact with the underside of the ice, i.e. with the charge 0 to 0.5 ft/lb$^{1/3}$ (0 to 0.2 m/kg$^{1/3}$) below the base of the ice cover. The probable radius of the resulting crater $R_c$ will then be

$$R_c \approx 6.56\ W^{1/3}\ \text{ft} \qquad \text{with } W \text{ in lb}$$

$$(23)$$

$$R_c \approx 2.6\ W^{1/3}\ \text{m} \qquad \text{with } W \text{ in kg}$$

A much simpler rule-of-thumb for optimum crater size is obtained by expressing dimensions as multiples of the ice thickness $t$. The charge depth $d_c$ (below the base of the ice) is then
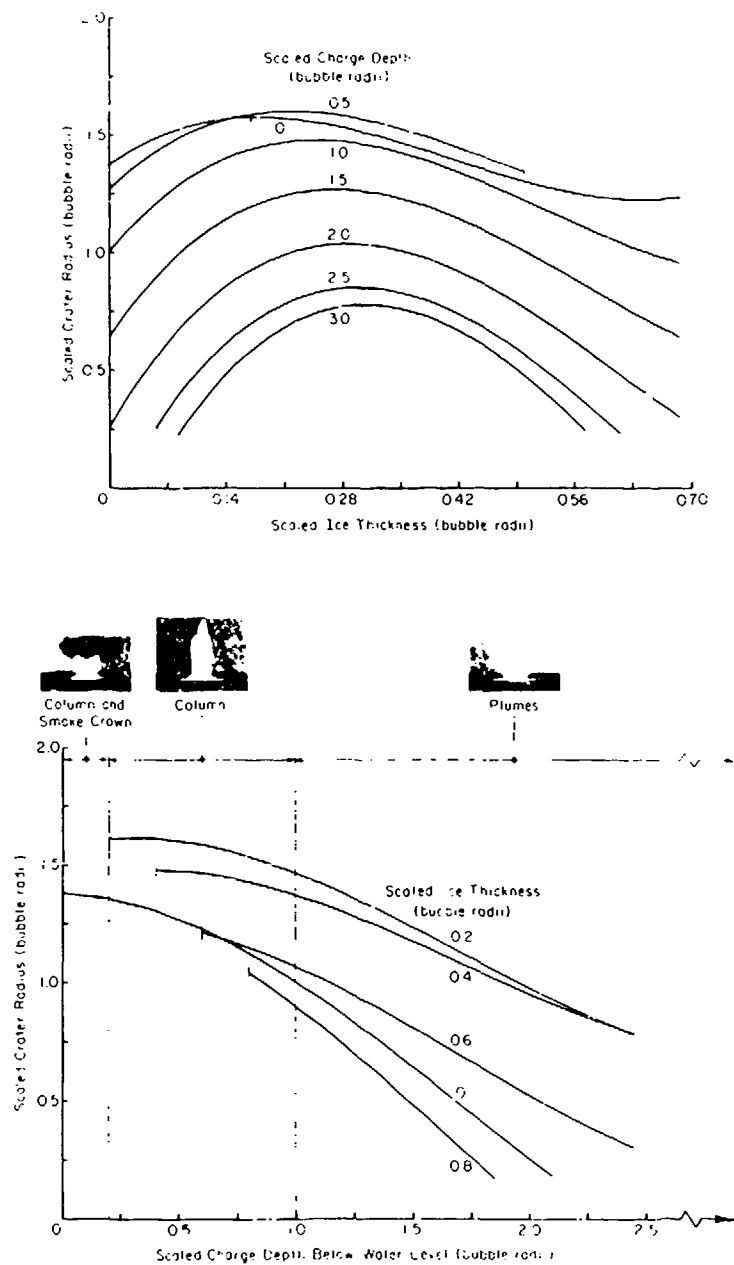
Figure 32. Prediction curves derived from regression analysis when linear dimensions are scaled with respect to maximum bubble radius, and water level is the depth datum.

$$d_c \approx 0 - 0.6 \, t \tag{24}$$

and the optimum crater diameter $D_c$ is

$$D_c = 2R_c \approx 15 \, t \, . \tag{25}$$

These guidelines are shown in Figure 33.

Optimum Charge Design
  α = 0 to 0.5
  W   14.5 in and 0.5
  W   21.1 kg and m.

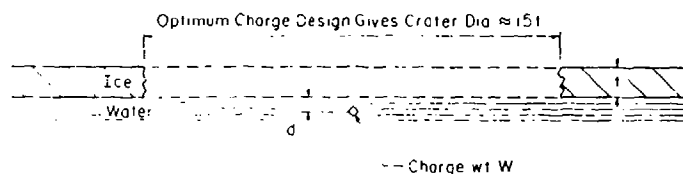Optimum Charge Design Gives Crater Dia ≈ 15t



Figure 33. Simple guidelines for optimum charge design (single crater).

The procedure just described gives the optimum value of W and the maximum value of $R_c$ when t is specified. In other applications (see Mellor 1982), the specified parameters may include W and a finite value of the charge depth $d_c$. In such cases, $t/W^{1/3}$ and $d_c/W^{1/3}$ are computed, so that $R_c$ can be estimated from Figure 31. Alternatively, t and $d_c$ may be given, leaving an optimum value of W to be estimated, largely on the basis of an optimum value of $t/W^{1/3}$ from Figure 31. Other variations of the problem can be dealt with, either directly or by iteration.

## Specific Energy, or Powder Factor, for Ice Fragmentation

The specific energy for fragmentation of a solid, $E_s$, is the energy consumed to break unit volume. The energy in a charge of weight W is kW, where k is a characteristic specific energy content for the particular explosive. k can be taken either as the heat of explosion, typically around 4.2 to 4.8 kJ/g for high explosives, or as the gas expansion energy, which is roughly 20% of the heat of explosion. The volume of ice broken by a single charge is $\pi R_c^2 t$, where $R_c$ is crater radius and t is ice thickness. Thus, for explosive icebreaking,

$$E_s = \frac{kW}{\pi R_c^2 t} = \frac{k/\pi}{(R_c/W^{1/3})^2 (t/W^{1/3})} . \qquad (26)$$

The weight of explosive per unit volume of fragmented material is known as the powder factor $F_p$, or as the specific charge. For ice blasting with a single charge:

41

$$F_p = \frac{W}{\pi R_c^2 t} = \frac{1}{\pi (R_c/W^{1/3})^2 \ (t/W^{1/3})} \quad . \qquad (27)$$

Figure 34 gives the specific charge (powder factor) as a function of scaled ice thickness for single charges at optimum depth, i.e. immediately below the bottom of the ice. The minimum value of specific charge is 0.0051 lb/ft$^3$, or 0.082 kg/m$^3$, and it is obtained when the scaled ice thickness is about 2 ft/lb$^{1/3}$, or 0.8 m/kg$^{1/3}$. In other words, the maximum specific <u>volume</u> of fragmentation occurs with $t/W^{1/3} \approx 2$ ft/lb$^{1/3}$ (0.8 m kg$^{1/3}$), whereas maximum specific <u>area</u> of fragmentation occurs with $t/W^{1/3} \approx 0.9$ ft/lb$^{1/3}$ (0.36 m/kg$^{1/3}$).

For comparison, the powder factor for optimum crater blasts in semi-infinite ice is about 0.01 to 0.02 lb/ft$^3$, or 0.004 to 0.008 kg/m$^3$.

Values of <u>specific energy</u> $E_s$ for explosive icebreaking by single charges can be obtained from F ure 34 by multiplying values of specific
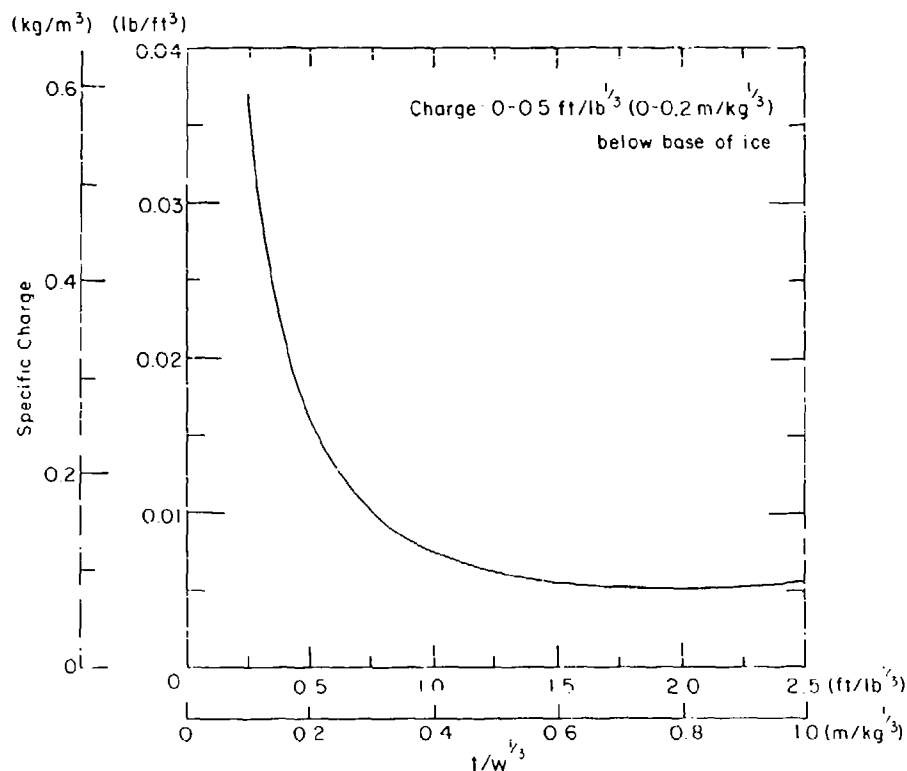


Figure 34. Specific charge, or powder factor, as a function of scaled ice thickness when single charges are at optimum depth.

42

charge by either the heat of explosion or the energy of gas expansion for explosive. The units of this specific energy are energy per unit volume, which reduces to the dimensions of a stress. If we take the heat of explosion as 4.6 kJ/g (1.1 kcal/g), which is about right for TNT, the minimum overall specific energy for explosive icebreaking is about 0.38 MJ/m$^3$, which is equivalent to 0.38 MPa (55 lbf/in.$^2$). This is comparable to the specific energy of a fairly large icebreaker (10,000-50,000 hp) when $E_s$ is based on shaft horsepower. The "process specific energy" for a ship, based on propeller thrust and speed, is lower, but this should be compared with an explosive specific energy that is based on the work of gas expansion (about 20% of the value given above).

The specific energy for maximum crater <u>area</u> is obtained by taking $(R_c/W^{1/3}) = 6.56$ ft/lb$^{1/3}$ and $(t/W^{1/3}) = 0.9$ ft/lb$^{1/3}$. These give $F_p = 0.0082$ lb/ft$^3$ (0.13 kg/m$^3$) and, with k = 4.6 kJ/g, $E_s = 0.6$ MJ/m$^3$ (0.6 MPa, 88 lbf/in.$^2$). If specific energy is based on the work of gas expansion, $E_s \approx 0.12$ MJ/m$^3$. These values are a bit higher than corresponding values for maximum specific <u>volume</u> of broken ice, but they are still comparable to the specific energy for an icebreaking ship.

## Cratering of Floating Ice by an Underwater Gas Bubble

Floating ice can be broken by a rapid gas discharge into the water beneath the ice. The gas bubble behaves much like that from a chemical explosive, but the initial pressure is relatively low and there is no transfer of intense shock to the surrounding water. Tests have been made with a variety of gas blasting systems, all of which discharge at relatively low pressure without propagating a true shock (Mellor 1984). Experimental equipment has included: (a) carbon dioxide shells (discharge pressure 70-90 MPa), (b) an airblasting system (69-83 MPa), (c) an air gun (17 MPa), and (d) a fuel/air combustion system (2.3-4.3 MPa).

Gas blasting results cannot be compared directly with explosives data. To draw any kind of conclusions from the limited data, dimensions have to be scaled with respect to the cube root of the discharge energy, which is taken as the energy for adiabatic gas expansion to atmospheric pressure. For comparison with explosives, it is not yet clear whether the energy of the conventional chemical explosive should be taken as the heat of explosion or as the energy of gas expansion. If a scaled dimension for gas blasting has units of m/MJ$^{1/3}$, it can be converted to units of m/kg$^{1/3}$

43

by multiplying by the cube root of an explosive specific energy factor that has units of MJ/kg. For TNT, the heat of explosion is approximately 4.56 MJ/kg and the energy of gas expansion is 0.87 MJ/kg; the corresponding cube root factors are 1.66 and 0.955 $(MJ/kg)^{1/3}$.

For ice-breaking gas discharges of magnitude 1 MJ, optimum scaled ice thickness for maximum crater diameter is about 0.4 $m/MJ^{1/3}$, optimum charge depth is in the range 0 to 0.6 $m/MJ^{1/3}$, and the resulting maximum crater radius is about 2.9 $m/MJ^{1/3}$ (Mellor 1984). If the gas expansion conversion factor for high explosives is applied to the optimum crater results for explosives (Fig. 31), the corresponding values are: optimum ice thickness 0.38 $m/MJ^{1/3}$, optimum charge depth 0 to 0.21 $m/MJ^{1/3}$, and maximum crater radius 2.7 $m/MJ^{1/3}$. Considering all the uncertainties that are involved, this is remarkably close agreement between gas blasting and explosives blasting. Furthermore, both gas blasting and chemical explosives give a probable maximum value for the scaled crater diameter of approximately 15 times the optimum ice thickness.

The specific energy $E_s$ for maximum values of scaled crater diameter is about 0.1 $MJ^{1/3}$. This is more or less the same as the corresponding specific energy for conventional explosives when $E_s$ is based on the work of gas expansion rather than upon the heat of explosion ($E_s \approx 0.12$ $MJ/m^3$).

This suggests that for optimum cratering the crater size is controlled by gas expansion and water displacement, not by shock propagation. Since much of the energy of a high explosive goes into gas expansion, and since the energy per unit mass of typical explosives does not vary between very wide limits, it also seems reasonable to expect that optimum crater dimensions will be fairly insensitive to explosive type. However, the degree of ice fragmentation within the crater is different for gas blasting devices and high explosives, and it seems probable that fragmentation will vary with explosive type. Gas blasting tends to give large fragments produced by a system of radial and circumferential cracks, while high explosives give more shattering in the central crater (Fig. 35).

If crater size is influenced mainly by gas expansion and water displacement, then variations in ice type might not have much effect. In particular, an ice cover formed by accumulation of ice fragments might respond much like an intact ice plate.
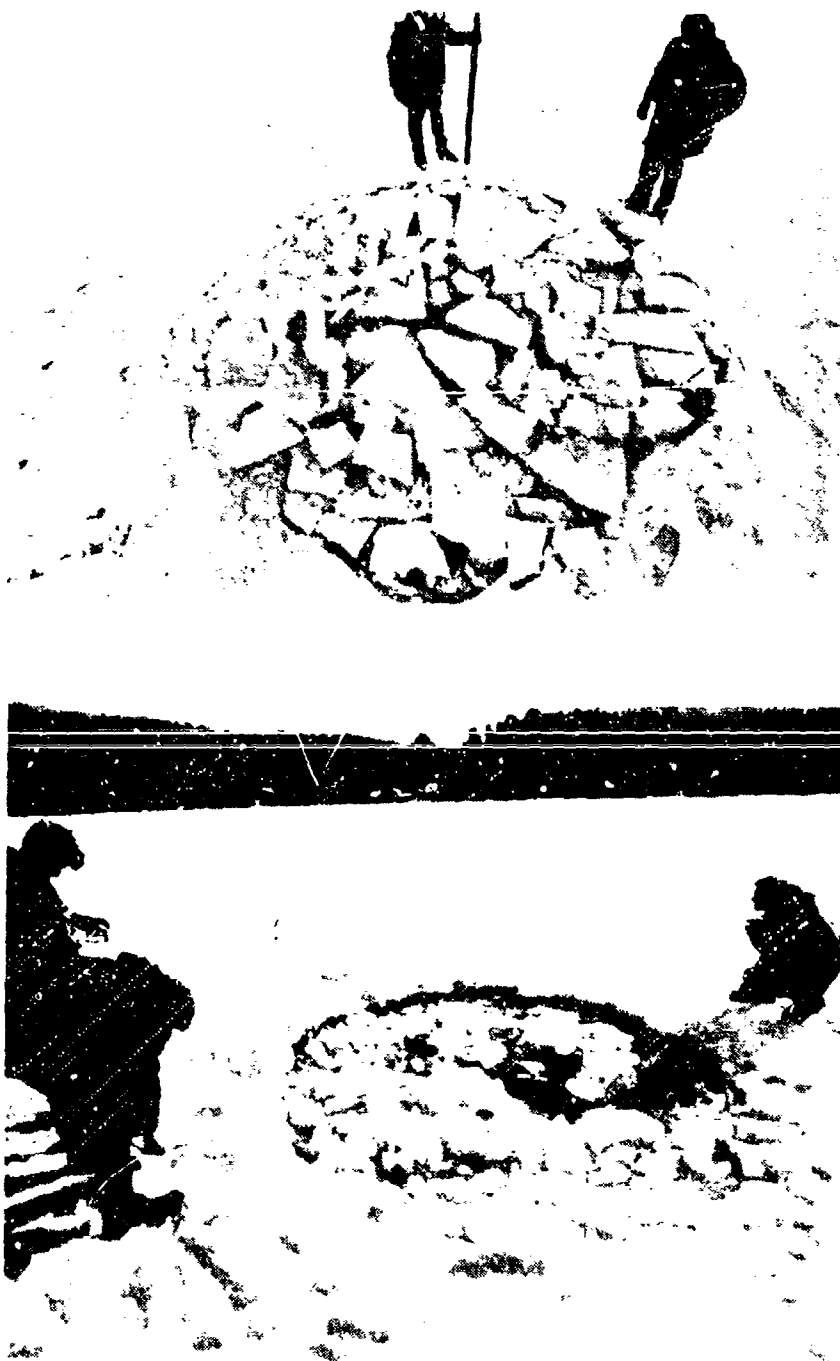
44

Figure 35. Comparison of ice fragmentation by gas discharge (top) and by high explosive (bottom).

45

## Use of Multiple Charges for Icebreaking

To break ice over wide areas, patterns of multiple charges can be used. A single line of charges, which could be used to open a channel, is termed a _row charge_. An array of multiple rows is called a _pattern charge_.

To design a row, or an array, of icebreaking charges, it is convenient to first calculate the crater radius $R_{c1}$ for a single charge and then to relate $R_{c1}$ to the spacing s for charges in a row, or in a square network.

In a _single row_ of charges where $s/R_{c1}$ is greater than about 2.5, or in an array where $s/R_c > 4$, each charge produces a separate eruption and a separate crater. When $s/R_{c1}$ becomes somewhat smaller than these values, each charge still gives a separate eruption (Fig. 36), but as the ice debris and the water columns fall back again, the ice between the individual craters is subjected to impact, base surge, and violent wave action. This can fracture the ice between the craters with varying degrees of fragmentation, depending on $s/R_{c1}$. Under these conditions, the author has chosen to accept 1 ft/lb$^{1/3}$ (0.4 m/kg$^{1/3}$) as optimum charge depth (instead of 0-0.5 ft/lb$^{1/3}$), in order to increase the base diameter of the water plume. There are no systematic data to support this judgment, which is based on data for waterspouts from ice-free surfaces.

Table 5. Effects of charges in a single row when each charge is close to optimum for the prevailing ice thickness, and charge depth is about 1t to 1.5t. Based on tests by Kurtz et. al. (1966), Fenstad and Gerard (1985), and unpublished work by the author.

| Charge spacing | Approximate width of fractured channel, b | | Fragmentation |
|---|---|---|---|
| $(s/R_{c1})$ | $(b/R_{c1})$ | $(b/s)$ | |
| >2.5 | Individual craters | | As for single crater |
| 2 | 3.8 | 1.9 | Poor at edges of channel and in cusps between craters |
| 1.5 | 3.4 | 2.3 | Good in mid-channel, less along edges |
| 1.0 | 3.4 | 3.4 | Good |

Figure 36. Shallow-depth multiple charges breaking through thin ice. Charge depth 0.45 bubble radii.

Drawing upon limited field data, probable effects of row charges are indicated in Table 5. The charges interact to produce a continuous broken channel when $s/R \leq 2.5$. Fragmentation improves and becomes more uniform as $s/R_{cl}$ decreases, until the row of individual charges approximates the effect of a continuous linear charge, for which the blast effects spread cylindrically rather than spherically.

A multi-row array produces more interference between craters, and the charge spacing can be wider than it is in a single row. The logical charge pattern is a square net of mesh size s. A "diamond," or "5-spot," pattern is obtained by rotating the reference axes of a square mesh through 45°. Limited personal experience with charge arrays indicates that individual craters are formed with $s/R_{c1} > 4$, continuous fracture occurs with $s/R_{c1} = 3$, adequate fragmentation is obtained with $s/R_{c1} = 2.7$, spacing is closer than necessary with $s/R_{c1} = 2.3$, and spacing is wastefully close with $s/R_{c1} = 2$. Fonstad and Gerard (1985) deduced an upper limit for useful interference as $s/R_{c1} = 3.5$, which agrees reasonably well with a value of 3.8 suggested earlier (Mellor 1982).

47

## Design of Multiple Charges for Breaking Thin Ice

If the ice is thin (< 1 ft; < 0.3 m), the optimum size of a single charge is small, and the absolute diameter of the resulting crater is also small (< 15 ft; < 4.5 m). When the objective is to break a wide channel or a broad area in thin ice with multiple charges, the required number of optimum charges may be large. Under these circumstances, the effort involved in drilling and charge emplacement can become excessive, and it may be more efficient in practical terms to use charges that are bigger than optimum, and to set them further apart.

Having made the calculations for optimum charge size to get a feel for things, a guess can be made at the total amount of explosive that seems affordable for the job, and a new charge size can be estimated (e.g. 5 lb instead of 1 lb, or 2.5 kg instead of 0.5 kg). The scaled ice thickness for the new charge weight is then calculated, and the curves of Figure 31 are used to obtain the corresponding value of $R_{c1}$ (perhaps taking a scaled charge depth of about 1 ft/lb$^{1/3}$ or 0.4 m/kg$^{1/3}$, as suggested earlier). Using the chosen value of $s/R_{c1}$, say 2.7, the new value of charge spacing s is obtained.

## Charges on Top of the Ice Sheet, or Inside It

A small charge placed on top of a thick ice sheet, or in its upper half, has much the same effect as a cratering charge in semi-infinite ice (Fig. 37). Figure 38 summarizes data for the scaled dimensions of the true
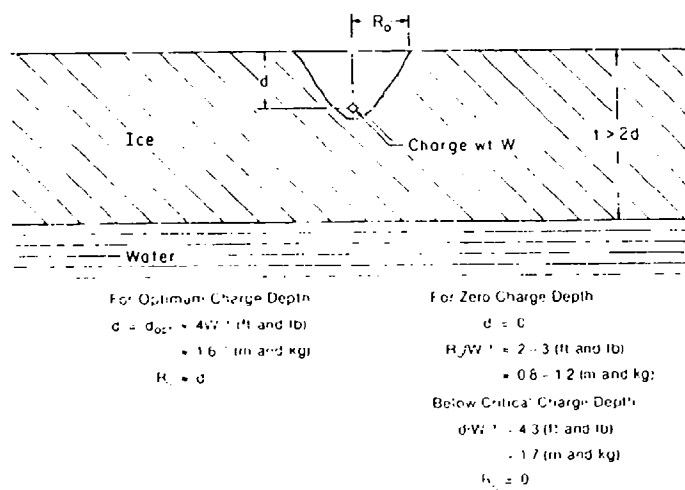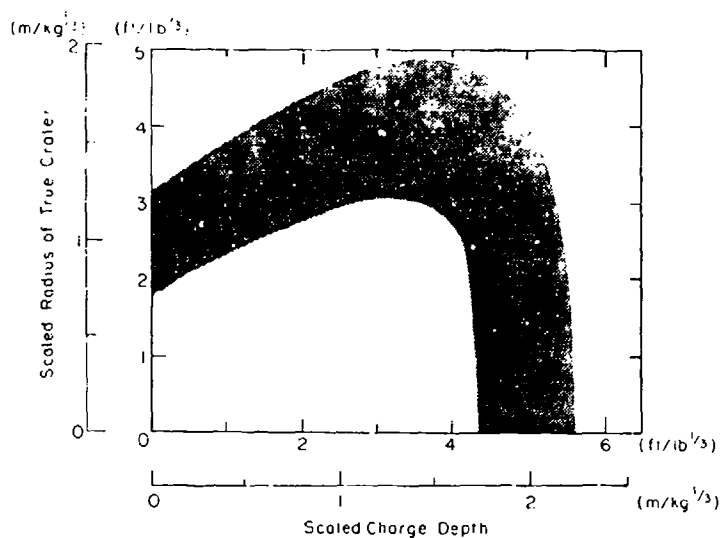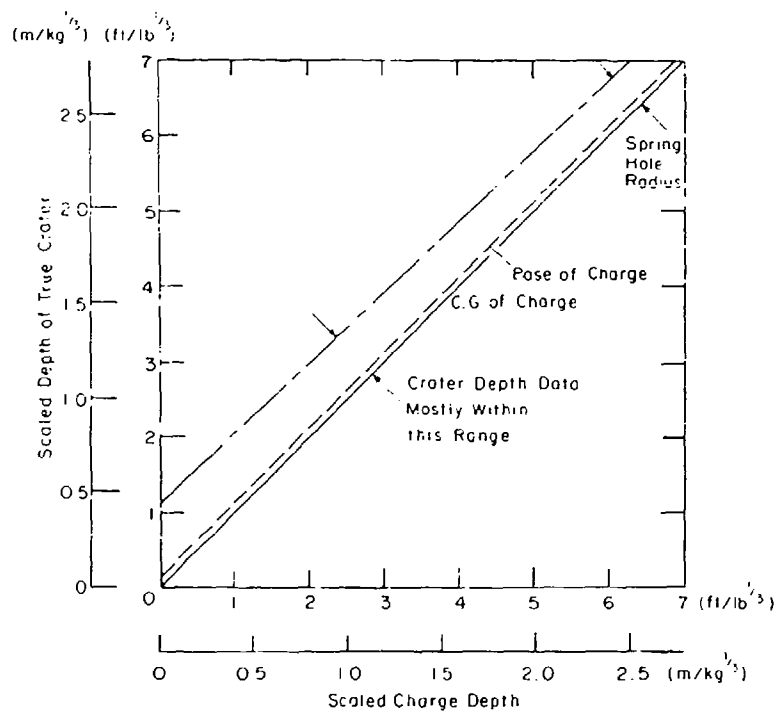


Figure 37. Summary of dimensions for the true crater produced by a small charge inside thick ice.

a. Scaled crater radius as a function of scaled charge depth.



b. Scaled crater depth as a function of scaled charge depth.

Figure 38. Summary of data for the scaled dimensions of the true crater in massive ice. Data from Livingston (1960).

crater in deep ice. The true crater is the more or less conical region of fractured ice, as distinct from the apparent crater, which is the visible open hole. The maximum scaled radius of the true crater, measured at the ice/air surface, is in the range 3 to 5 $ft/lb^{1/3}$ (1.2 to 2.0 $m/kg^{1/3}$). This maximum is achieved with a scaled charge depth of 3 to 4 $ft/lb^{1/3}$ (1.2 to 1.6 $m/kg^{1/3}$). In other words, the true crater for optimum charge depth is equivalent to a cone with a 45° half-angle.

Corresponding data for the apparent crater are given in Figure 39. Dimensions of the apparent crater are smaller than those of the true crater because some of the fractured ice is not grossly displaced, and some ejected fragments fall back into the crater.

A charge set at, or below, mid-depth can break out to both the ice/air and the ice/water interfaces, provided that $t/2W^{1/3}$ is less than about 4 $ft/lb^{1/3}$ (1.6 $m/kg^{1/3}$). However, the maximum scaled radius of the upper or lower surface fracture zone is likely to drop below the 3-5 $ft/lb^{1/3}$ (1.2-2.0 $m/kg^{1/3}$) value for an optimum cratering charge in very thick ice.

To cut a relatively narrow vertical shaft through thick ice, delayed deck charges can be employed. Several charges are placed at different depths, and they are fired in rapid sequence, from top to bottom with appropriate delays (Fig. 40). The top charge is designed to produce the required hole diameter, in accordance with the cratering data of Figure 38. Successive charges vent through this crater, and a final charge in the water beneath the ice flushes out ice fragments. An alternative is to place a well-coupled line charge in a vertical drill hole, with a delayed charge in the water to flush out fragments.

When a small unconfined charge is laid on top of thick ice it makes a superficial crater, with the dimensions given by Figures 38 and 39 for zero charge depth. The scaled radius of the true crater is 2-3 $ft/lb^{1/3}$ (0.8-1.2 $m/kg^{1/3}$) at the surface, but the depth is small, say 0.6 to 1.0 $ft/lb^{1/3}$ (0.24 to 0.4 $m/kg^{1/3}$). In order for a surface charge to break through to the bottom of the ice sheet and to form a penetration crater, as in Figure 41, the scaled ice thickness has to be less than 2 $ft/lb^{1/3}$ (0.8 $m/kg^{1/3}$). As the scaled ice thickness decreases, the radius of the crater increases, but it is always much smaller than the radius of the crater that would be produced by the same charge set in water under the
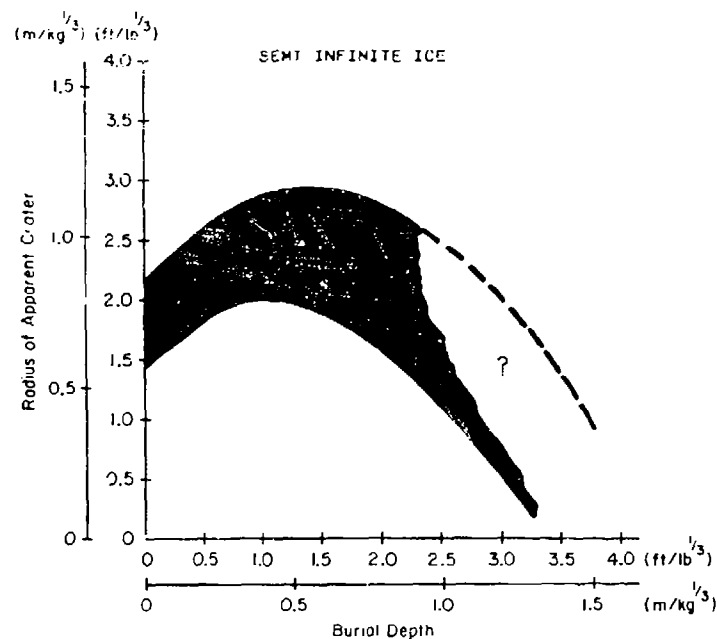
50

a. Scaled crater radius as a function of scaled charge depth.
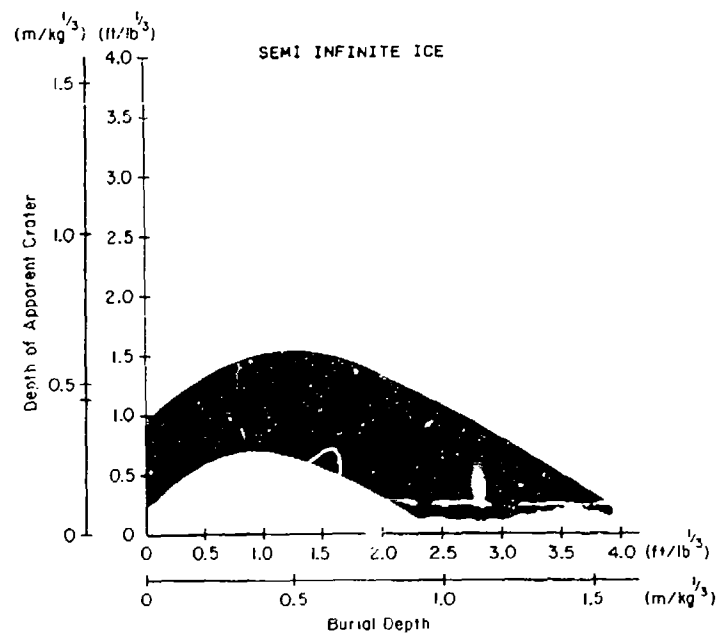


b. Scaled crater depth as a function of scaled charge depth.

Figure 39. Summary of scaled dimensions for apparent craters in massive ice. Data from Livingston (1960)

#1 Small cratering charge to control hole diameter

#2 Larger charge venting through crater of #1

#3 Charge venting upward and also breaking to base of ice

#4 Relatively large clearing charge below ice

Charges fired in sequence with delays in order to produce narrow hole and to clear debris from hole.
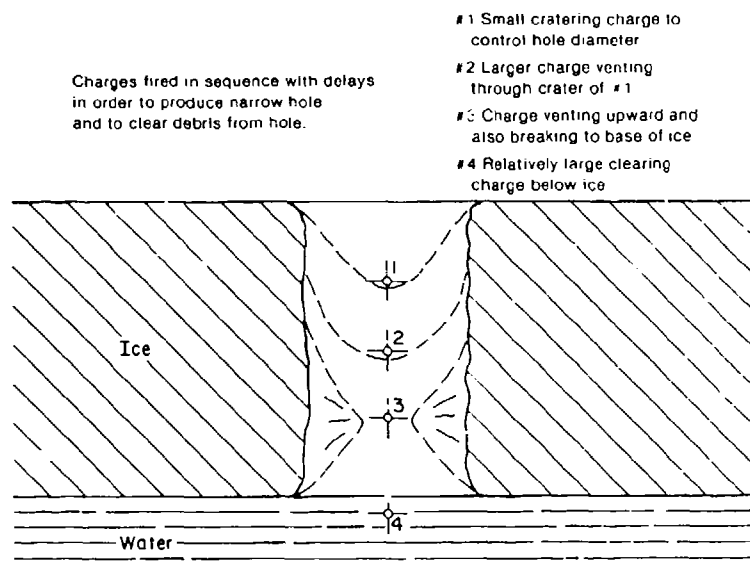
Figure 40. Use of delay deck charges to break a narrow shaft through very thick ice.
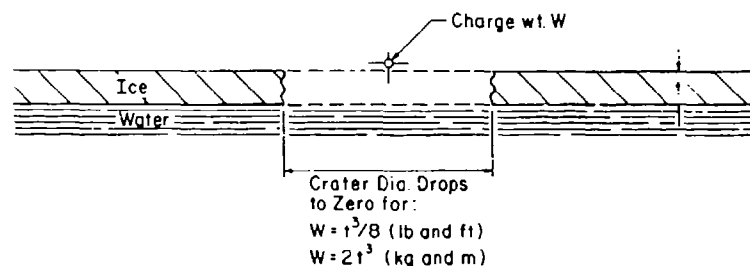
Figure 41. Effect of a charge lying on the upper surface of thin ice.

base of the ice sheet (Fig. 42). A surface charge is likely to produce more breakage if it is covered by sandbags, or mudcapped in some other way.

A charge in air above the ice surface is even less effective than a surface charge. No systematic test results have been reported, but at a scaled ice thickness of 1 ft/lb$^{1/3}$ (0.4 m/kg$^{1/3}$), no crater is formed when the charge height is 0.5 ft/lb$^{1/3}$ (0.2 m/kg$^{1/3}$) or more.
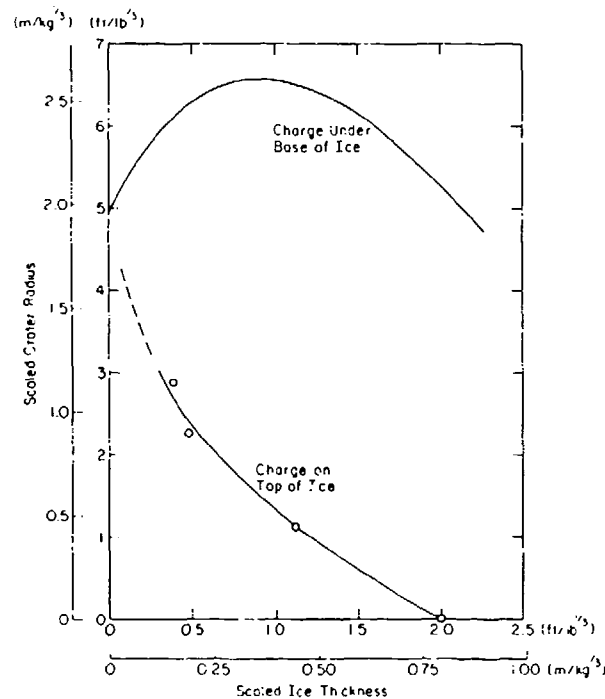
Figure 42. Effects of surface charges compared with the effects of under-ice charges. Data for surface charges from Barash (1966) and Fonstad et al. (1981).

## The Physical Basis of Explosive Icebreaking

While it is easy to identify the physical phenomena involved in explosive icebreaking, the relative significance of the various effects is less easy to deduce from abstract considerations. We therefore have to examine the test data, taking advantage of the admittedly imperfect empirical correlations described in the previous sections.

Surveying the general body of field test results, certain facts emerge:

1. High explosives and gas blasting devices produce craters of about the same size (D ≈ 15 t) when the blast is properly optimized, but high velocity explosives give greater fragmentation in the central crater.

2. For high explosives, the crater diameter in __thin__ ice correlates with the maximum theoretical diameter of the gas bubble, and with the base diameter of the erupting water column (Fig. 43).

3. Underwater explosions break ice most effectively in the range where columnar eruptions would occur under ice-free conditions (Fig. 32).
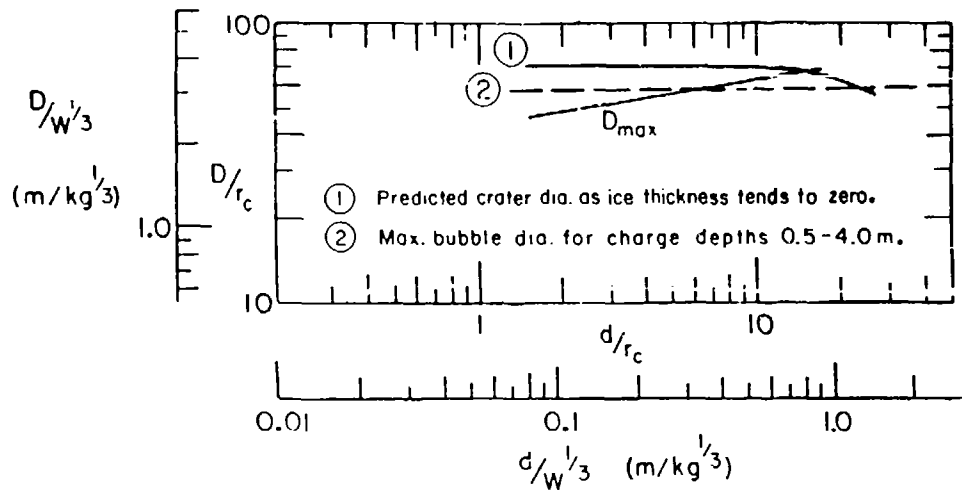
Figure 43. Predicted crater diameter in very thin ice compared with the scaled dimensions of explosive eruptions from an ice-free water surface.

4. Crater dimensions are not much affected by variation of explosive type (linear dimensions vary with the cube root of the explosive's specific energy).

5. The maximum crater diameter for explosions is smaller than the diameter of cracking for slow, radially symmetric flexure of an ice sheet. For ice 1 m thick, the blast crater diameter is about 15 m, whereas the diameter of the outermost circumferential crack for flexure might be 50 to 70 m.

6. The specific energy $E_S$ for explosive icebreaking is very much higher than the specific energy for icebreaking by slow flexure. A blast optimized for maximum crater diameter might give $E_S \approx 0.5$ MJ/m$^3$ when it is based on heat of explosion (Fig. 34), or $E_S \approx 0.1$ MJ/m$^3$ when it is based on the work of gas expansion. By contrast, slow flexure by a concentrated force could give $E_S$ in the range 2 to 700 J/m$^3$, depending on displacement rate.

7. The specific energy for optimized gas blasting devices ($E_B \approx 0.1$ MJ/m$^3$) is the same as the specific energy for high explosives when the explosive energy is taken as the work of gas expansion (about 20% of the heat of explosion).

From these observations, the following tentative conclusions might be drawn:

1. Maximum crater size is controlled more by eruptions driven by the gas bubble than by shock wave shattering of the ice.

2. Since the specific energy for cratering is the same for explosives and gas blasting devices when $u_s$ is based on gas expansion energy, some of the total energy of a high explosive may be wasted in ice cratering.

3. Variation of explosive type is not very important in determining crater size.

4. Craters in ice are formed by local high speed piercing rather than by widespread flexural doming, although there is an annulus around the crater where the ice breaks by flexure.

If these conclusions are valid, then it should be possible to compile and correlate test data with closer regard to the physics of the process. For typical explosives and moderate charge sizes (say up to 500 kg), cube root scaling can be retained, and variation of explosive type can be ignored, or adjusted on the basis of specific energy. If bubble expansion is the dominant effect, charge depth ought to be referred to the water surface rather than the underside of the ice cover. As an alternative to cube root scaling, especially if very large explosions are being considered, linear dimensions of the problem could be scaled with respect to the theoretical maximum bubble radius. Both of these changes to the data handling scheme have been tried, but the net result in both cases is a deterioration in the empirical correlations. For the time being, the simple scheme outlined earlier is still in use for practical purposes.

LITERATURE CITED

Barash, R.M. (1966a) Ice-breaking by explosives. U.S. Naval Ordnance Laboratory, White Oak, Silver Spring, Maryland, NOLTR 66-229.

Barash, R.M. (1966b) Measurement of underwater explosion pulses reflected from an ice layer. In unpublished report, Office of Naval Research, Code 468.

Cole, R.H. (1948) Underwater Explosions. Princeton University Press (republished in 1965 by Dover Publications), 437 pp.

Fonstad, C.D. and R. Gerard (1985) Field tests of techniques for explosive cratering of floating ice sheets. In Proceedings, Annual Conference, Canadian Society for Civil Engineering, Saskatoon, p. 341-363.

Glasstone, S. (Ed.) (1962) The effects of nuclear weapons. DA Pamphlet 39-3, 730 pp.

Johansson, C.H. and P.A. Persson (1970) Detonics of High Explosives. London and New York: Academic Press, 330 pp.

Kurtz, M.K., R.H. Benfer, W.G. Christopher, G.E. Frankenstein, G. Van Wyne and E.A. Roguski (1966) Consolidated report, Operation Break-up, FY66. Ice cratering experiments, Blair Lake, Alaska. Nuclear Cratering Group, Lawrence Radiation Laboratory, Livermore, California, NCG/TM 66-7 (reprinted in River Ice Jams, S.J. Bolsenga, ed., 1968, Research Report 5-5, U.S. Lake Survey, Detroit).

Livingston, C.W. (1960) Explosions in ice. U.S. Army Snow, Ice and Permafrost Research Establishment, Technical Report 75, AD-276605.

Mellor, M. (1972) Data for ice blasting. USA Cold Regions Research and Engineering Laboratory, Technical Note (unpublished).

Mellor, M. (1982) Breaking ice with explosives. USA Cold Regions Research and Engineering Laboratory, CRREL Report 82-40.

Mellor, M. (1984) Icebreaking by gas blasting. IAHR Ice Symposium, Hamburg.

Mellor, M. (1986) Derivation of guidelines for blasting floating ice. USA Cold Regions Research and Engineering Laboratory, Special Report 86-10.

Slifko, J.P. (1967) Pressure pulse characteristics of deep explosions as a function of depth and range. U.S. Navy NOLTR 67-87 (quoted by Swisdak, 1978, but not seen by this author).

Snay, H.G. (1957) Hydrodynamics of underwater explosions. In Symposium on Naval Hydrodynamics, Office of Naval Research and National Research Council, NAS/NRC publication 515, p. 325-352.

Swisdak, M.M. (1978) Explosion effects and properties. Part II: Explosion effects in water. Naval Surface Weapons Center, Technical Report 76-116, 109 pp.

Young, G.A. (1971) The physical effects of conventional explosions on the ocean environment. U.S. Naval Ordnance Laboratory, White Oak, Silver Spring, Md., NOLTR 71-120 (distribution unlimited).

Young, G.A. (1973) Plume and ejecta hazards from underwater explosions. U.S. Naval Ordnance Laboratory, White Oak, Silver Spring, Md., NOLTR 73-111 (limited distribution - results may be quoted in open literature).